

Beyond Linearity: Squeeze-and-Recalibrate Blocks for Few-Shot Whole Slide Image Classification

Conghao Xiong¹ Zhengrui Guo² Zhe Xu¹ Yifei Zhang³ Raymond Kai-Yu Tong¹
Si Yong Yeo^{4,5} Hao Chen² Joseph J. Y. Sung⁵ Irwin King¹

¹CUHK ²HKUST ³NTU ⁴MedVisAI Lab ⁵Lee Kong Chian School of Medicine, NTU
Email: {chxiong21, king}@cse.cuhk.edu.hk

Abstract

Deep learning has advanced computational pathology but expert annotations remain scarce. Few-shot learning mitigates annotation burdens yet suffers from overfitting and discriminative feature mischaracterization. In addition, the current few-shot multiple instance learning (MIL) approaches leverage pretrained vision-language models to alleviate these issues, but at the cost of complex preprocessing and high computational cost. We propose a Squeeze-and-Recalibrate (SR) block, a drop-in replacement for linear layers in MIL models to address these challenges. The SR block comprises two core components: a pair of low-rank trainable matrices (squeeze pathway, SP) that reduces parameter count and imposes a bottleneck to prevent spurious feature learning, and a frozen random recalibration matrix that preserves geometric structure, diversifies feature directions, and redefines the optimization objective for the SP. We provide theoretical guarantees that the SR block can approximate any linear mapping to arbitrary precision, thereby ensuring that the performance of a standard MIL model serves as a lower bound for its SR-enhanced counterpart. Extensive experiments demonstrate that our SR-MIL models consistently outperform prior methods while requiring significantly fewer parameters and no architectural changes.

1 Introduction

Histopathological image analysis is the gold standard for cancer diagnosis and prognosis. Recently, deep learning has achieved clinical-grade performance in various tasks [4, 13, 33, 39, 48, 49, 50]. However, the gigapixel dimensions of Whole Slide Images (WSIs) render their direct processing by neural networks infeasible, making Multiple Instance Learning (MIL) the de facto strategy. In this framework, WSIs are divided into patches (instances), and features are extracted from these patches using pretrained models (*e.g.*, ResNet [17]). The resulting features subsequently serve as inputs for MIL models. In addition, annotating the gigapixel WSIs requires extensive expertise and considerable time from pathologists, resulting in data scarcity. This poses a significant challenge for deep learning models, which typically demand abundant annotated data to reach optimal performance [15].

Few-shot learning enables models to generalize from only a handful of labeled examples, typically by leveraging prior knowledge [32, 44]. Following this principle, recent MIL-based Vision-Language Models (VLMs) show promise under few-shot settings, whether built on pretrained CLIP backbones [36, 37] or adapted from Large Language Models (LLMs) [15, 27, 40]. However, these VLM methods depend on *complex preprocessing pipelines* (multi-resolution patch generation [40] and fine-grained description generation [11, 27]), incur *substantial parameter overhead* [40], and demand *customized MIL architectures* to integrate language priors [11, 15, 27, 40, 36, 37]. Furthermore, their performance is highly contingent on the choice of pretrained model, and, together with the factors discussed previously, these disadvantages compromise their feasibility for clinical implementation.

In practice, both MIL and the recent VLM methods face two learning challenges: *the overfitting tendency* [53] and *the difficulty of locating discriminative features* [42, 44]. First, models, particularly parameter-intensive VLMs, are prone to overfitting, a problem that the gigapixel WSIs exacerbates, creating an extreme large-p, small-n scenario [41]. Second, when training data are scarce, models often learned spurious shortcut correlations, such as variations in patch color [3], rather than genuine discriminative patterns, which undermines their ability to learn robust and generalizable features [3].

To address these challenges, we propose a novel paradigm for few-shot learning in computational pathology: replacing the linear layer in the MIL models with our Squeeze-and-Recalibrate (SR) block. Specifically, our SR block comprises two trainable low-rank matrices with an activation function in between (Squeeze Pathway, SP), and a randomly-initialized frozen matrix (recalibration matrix).

Empirically, our SR block overcomes all of the aforementioned challenges by seamlessly slotting into MIL models without any modifications, thereby eliminating the complex preprocessing and excessive parameter overhead associated with VLM approaches. In addition, its two components offer further advantages: the SP reduces the number of trainable parameters, mitigating overfitting, and its low-rank constraint imposes a bottleneck that compels the network to focus on the discriminative features; meanwhile, the recalibration matrix, though randomly initialized and untrained, 1) preserves geometry while diversifying feature directions, similar to extreme learning machine [22, 38], and 2) redefines the optimization objective for SP as fitting the residual to the random scaffold [8, 9, 10, 17, 18, 54].

Theoretically, our SR block is justified by two complementary results that both rely on the recalibration matrix properties. We first prove that the SR block can approximate any linear layer with arbitrary precision (Sec. 3.2.1). This guarantees that the performance achieved by a MIL model with linear layers serves as a lower bound for the corresponding SR-MIL model, because in the event that the SR-MIL model does not identify superior model parameters, it can still replicate the behavior of the linear layer and thus attain comparable performance. We then show that the random recalibration matrix preserves the geometry of the input features while expanding them into additional directions, thereby enriching their representation (Sec. 3.2.2). These results are possible because a random sub-Gaussian matrix is almost surely invertible (Appendix C.1) and has tightly concentrated singular values (Sec. 3.2.1), which ensures full-rank coverage and allows the SP output to be *recalibrated* to a full dimensional space that diversifies the features. Furthermore, with this full-rank scaffold, the SP only need to fit the residual, and based on the Eckart–Young–Mirsky theorem, a rank r truncated SVD is guaranteed to yield a solution that minimizes the Frobenius norm of that residual. These properties underpin both the approximation guarantee and the feature diversification of the SR block.

The contributions of this work can be summarized as follows:

1. We pioneer a new paradigm for few-shot computational pathology by introducing a novel drop-in SR block that curbs overfitting, prevents spurious feature learning, removes complex preprocessing, and improves performance without any MIL architectural modifications.
2. We provide theoretical justification that the linear-layer MIL serves as the worst-case baseline for SR-MIL counterparts, and the recalibration matrix enriches the input features.
3. We conduct extensive experiments, including comparative experiments, ablation studies, and sensitivity analyses, to validate both the efficacy and efficiency of our method.

2 Related Work

2.1 Multiple Instance Learning

MIL has emerged as the predominant framework for processing gigapixel WSIs. In a typical MIL pipeline, WSIs are tessellated into small patches, which are then input into a pretrained neural network. Historically, architectures such as ResNet-50 [17] have been employed; however, there is an increasing trend toward using pathology-specific pretrained foundation models, such as UNI [4] and CONCH [32] (Sec. 2.2). Based on the method used to derive the final classification logits, MIL approaches can be broadly categorized into two streams: *instance-level* approaches and *embedding-level* approaches. In the instance-level paradigm, logits are first computed for each patch and then aggregated to yield a slide-level prediction [2, 5, 21, 26]. Conversely, embedding-level approaches first aggregate patch features via pooling or aggregator networks to form a slide-level embedding, which is subsequently used to generate the final prediction [14, 23, 25, 29, 28, 33, 39, 43, 48, 52].

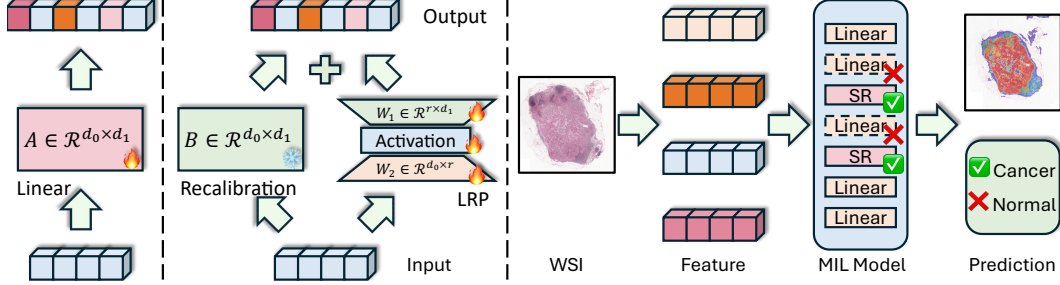


Figure 1: Illustration of the linear transformation (left), our proposed SR block (middle), and the overall pipeline of MIL for WSI classification task and where our SR block takes effect (right).

2.2 Pathology Foundation Model

Traditional feature extraction relies on ImageNet-pretrained ResNet [7, 17]. However, the domain shift between natural images and WSIs, *e.g.*, unique tissue organizations, staining variability, and intricate details, limits their efficacy in pathology domain. To address these challenges, both pure vision and vision-language pathology foundation models have been developed [47]. For example, Virchow [45], UNI [4], and GPFM [35] are pretrained on extensive pathology datasets without text modalities, and VLMs, including PLIP [24], CONCH [32], and MUSK [46], leverage image-text pairs to enhance multimodal tasks. Notably, mSTAR [51] integrates WSIs with reports and genomic data, enriching feature representations. These pathology foundation models, which encapsulate extensive pathology knowledge, enable few-shot WSI classification and advance computational pathology.

2.3 Few-shot Weakly-supervised Learning for WSI Classification

Few-shot weakly-supervised learning (FSWSL) was initially introduced in TOP [36], and subsequent studies [11, 15, 27, 37, 40] have further expanded on this paradigm. This approach is especially appealing in the pathology due to the substantial costs and labor associated with high-quality annotations. Current FSWSL methods typically employ computationally intensive components, such as CLIP and other LLMs, to achieve competitive performance. In contrast, our method is designed as a universal, on-the-fly plugin that is compatible with any existing MIL models, including ABMIL-based [23, 25, 52] and transformer-based [39] methods. This design not only enhances generalizability and computational efficiency but also broadens the applicability of few-shot learning in clinical settings.

3 Methodology

We begin with MIL formulation, then introduce our SR block, establish its worst-case performance guarantee, and demonstrate that the recalibration matrix preserves the input feature characteristics.

3.1 Multiple Instance Learning Formulation

In MIL, given a WSI, we first partition it into N non-overlapping patches. Each patch is then passed through a pretrained neural network to produce a feature vector $\mathbf{f}_i \in \mathbb{R}^{d_p}$, where d_p is the output dimension. Next, we apply an MIL model to aggregate the stacked patch-level features $\mathbf{F} = \{\mathbf{f}_i\}_{i=1}^N$ into the bag-level feature $\mathbf{f} = \text{MIL}(\mathbf{F}) \in \mathbb{R}^{d_f}$, where d_f is the dimension of the bag feature. Finally, this bag feature is fed into a classifier to obtain the slide-level logits $\mathbf{p} = \text{CLS}(\mathbf{f}) \in \mathbb{R}^C$ with C being the number of classes. Importantly, most MIL models use attention pooling to compute \mathbf{f} , yielding the bag-level feature and per-patch importance scores. The MIL framework is shown in Fig. 1 (right).

3.2 Squeeze-and-Recalibrate Block

To mitigate overfitting and learning spurious features, we propose a novel paradigm, in which the linear layer is substituted with our SR block. This enhances model performance and reduces the trainable parameter count without requiring complex preprocessing or redesigning of the MIL architectures. Figure 1 illustrates 1) the linear layer, 2) our SR block, and 3) the process that our SR

block slots into the MIL models. Intuitively, our SR block splits the linear layer into a frozen random recalibration matrix that preserves geometry plus a pair of learnable low-rank correction matrices. Given the input $\mathbf{X} \in \mathbb{R}^{N \times d_0}$ with the input feature dimension being d_0 , and the “ideal” linear layer $\mathbf{A}_* \in \mathbb{R}^{d_0 \times d_1}$ to be approximated, our SR block $f_{SR} : \mathbb{R}^{d_0} \rightarrow \mathbb{R}^{d_1}$ can be expressed by,

$$\mathbf{X} \mathbf{A}_* \approx f_{SR}(\mathbf{X}) = \text{Activation}(\mathbf{X} \mathbf{W}_2) \cdot \mathbf{W}_1 + \mathbf{X} \mathbf{B}, \quad (1)$$

where $\text{Activation}(\cdot)$ denotes a chosen activation function, $\mathbf{W}_1 \in \mathbb{R}^{r \times d_1}$ and $\mathbf{W}_2 \in \mathbb{R}^{d_0 \times r}$ are the SP, r is the rank parameter satisfying $r < (d_0 d_1)/(d_0 + d_1)$, and $\mathbf{B} \in \mathbb{R}^{d_0 \times d_1}$ is the Kaiming-uniform-initialized [16] random recalibration matrix, the default scheme for the linear layer.

Space Complexity Analysis. In the linear layer, the matrix \mathbf{A}_* contains $d_0 d_1$ trainable parameters; however, in our approach, as \mathbf{B} is frozen, the only trainable part is SP, with $(d_0 + d_1)r$ trainable parameters. Defining the reduction ratio $r_r = (d_0 + d_1)r/(d_0 d_1)$, and enforcing $r_r < 1$, yields the constraint $r < (d_0 d_1)/(d_0 + d_1)$. If $r_r \geq 1$, the trainable parameter count in the SR block would match or exceed $d_0 d_1$, the trainable parameter count in \mathbf{A}_* , which makes our SR block meaningless.

Time Complexity Analysis. The forward-pass cost of a linear layer scales as $\mathcal{O}(d_0 d_1)$, whereas our SR block incurs an additional low-rank branch, yielding $\mathcal{O}(d_0 d_1 + (d_0 + d_1)r)$. During back-propagation, the linear layer again requires $\mathcal{O}(d_0 d_1)$ complexity for both weight- and input-gradient computation. In contrast, our SR block only propagates gradients through its trainable pathway, at a cost of $\mathcal{O}((d_0 + d_1)r)$, matching its parameter count. Full derivations are provided in Appendix A.

3.2.1 Proof of Approximation Capabilities of Squeeze-and-Recalibrate Block

In this section, we prove that our SR block can approximate any linear layer to arbitrary precision, thereby providing a worst-case performance guarantee: if the SR block cannot improve over the linear layer then it can match its behavior arbitrarily closely, ensuring no loss in worst-case performance. In addition, rather than directly proving our formulation, we establish a more fundamental result without activation functions. Subsequently, with the universal approximation theorem [1, 6, 12, 20, 34], our architecture with non-linear activation function can achieve even superior approximation precision.

Theorem 1 (Universal Approximation by Squeeze-and-Recalibrate Block). *Let $\mathbf{A}_* \in \mathbb{R}^{d_0 \times d_1}$ have full rank $r_A = \min\{d_0, d_1\}$. Draw a frozen matrix $\mathbf{B} \in \mathbb{R}^{d_0 \times d_1}$ with sub-Gaussian entries. Then almost surely: for every $\varepsilon > 0$ there exist integers $r \leq r_A$ and matrices \mathbf{W}_2 and \mathbf{W}_1 such that,*

$$\|\mathbf{A}_* - (\mathbf{B} + \mathbf{W}_2 \mathbf{W}_1)\|_F \leq \varepsilon, \text{ where } \mathbf{W}_2 \in \mathbb{R}^{d_0 \times r}, \text{ and } \mathbf{W}_1 \in \mathbb{R}^{r \times d_1}. \quad (2)$$

Proof. Full-Rank Guarantees and Singular-Value Bounds. We prove that \mathbf{B} is full rank almost surely in Appendix C.1. Let $\delta, \eta \in (0, 1)$, according to Johnson–Lindenstrauss Lemma, we have,

$$(1 - \delta)\|\mathbf{x}\|_2 \leq \frac{1}{\sqrt{d_0}}\|\mathbf{B} \mathbf{x}\|_2 \leq (1 + \delta)\|\mathbf{x}\|_2 \implies \forall \sigma(\mathbf{B}) \in [\sqrt{d_0}(1 - \delta), \sqrt{d_0}(1 + \delta)], \quad (3)$$

with probability at least $1 - \eta$, if the input dimension satisfies $d_0 \geq C(d_1 + \ln(1/\eta))/\delta^2$.

Truncated SVD of the Residual. Let $\mathbf{E} = \mathbf{A}_* - \mathbf{B}$. Its singular value decomposition is given as $\mathbf{E} = \mathbf{U} \mathbf{\Sigma} \mathbf{V}^\top$. By the Eckart–Young–Mirsky theorem, we choose $r \leq r_A$ and we have,

$$\|\mathbf{E} - \mathbf{E}_r\|_F = \sqrt{\sum_{i=r+1}^{\text{rank}(\mathbf{E})} \sigma_i^2(\mathbf{E})} \leq \varepsilon, \text{ where } \mathbf{E}_r = \sum_{i=1}^r \sigma_i \mathbf{u}_i \mathbf{v}_i^\top. \quad (4)$$

Low-rank Correction Construction. From the last step, we can set \mathbf{W}_1 and \mathbf{W}_2 as,

$$\mathbf{W}_2 = [\mathbf{u}_1, \dots, \mathbf{u}_r] \mathbf{\Sigma}_r^{1/2}, \quad \mathbf{W}_1 = \mathbf{\Sigma}_r^{1/2} [\mathbf{v}_1, \dots, \mathbf{v}_r]^\top, \text{ where } \mathbf{\Sigma}_r = \text{diag}(\sigma_1, \dots, \sigma_r), \quad (5)$$

which satisfies $\mathbf{W}_2 \mathbf{W}_1 = \mathbf{E}_r$ and therefore, for sufficiently large r , we have

$$\|\mathbf{A}_* - (\mathbf{B} + \mathbf{W}_2 \mathbf{W}_1)\|_F = \|\mathbf{E} - \mathbf{E}_r\|_F < \varepsilon. \quad (6)$$

□

3.2.2 Proof of Characteristic Preserving of Random Matrix

Rather than disrupting the feature properties, the recalibration matrix preserves their geometric structure of the input feature vectors and enriches the feature diversity while retaining the prior knowledge. Due to space constraint, we prove these properties in Appendix B.

Table 1: Experimental results comparing our proposed method with baseline approaches are presented under various shot settings across Camelyon16, TCGA-NSCLC and TCGA-RCC dataset. Performance metrics in which our method outperforms the baseline are highlighted in bold red.

k	Methods	#P	Camelyon16			TCGA-NSCLC			TCGA-RCC		
			AUC \uparrow	F1 \uparrow	Acc. \uparrow	AUC \uparrow	F1 \uparrow	Acc. \uparrow	AUC \uparrow	F1 \uparrow	Acc. \uparrow
1	ViLaMIL [40]	40.7	0.651 _{0.009}	0.468 _{0.147}	0.679 _{0.059}	0.618 _{0.058}	0.622 _{0.055}	0.640 _{0.032}	0.859 _{0.039}	0.664 _{0.048}	0.695 _{0.063}
	ABMIL [25]	0.26	0.551 _{0.070}	0.491 _{0.107}	0.571 _{0.078}	0.679 _{0.059}	0.618 _{0.058}	0.622 _{0.055}	0.761 _{0.141}	0.575 _{0.167}	0.614 _{0.177}
	SR-ABMIL	0.18	0.594 _{0.124}	0.508 _{0.082}	0.628 _{0.028}	0.702 _{0.099}	0.591 _{0.065}	0.610 _{0.049}	0.734 _{0.073}	0.540 _{0.092}	0.523 _{0.086}
	CLAM [33]	0.53	0.629 _{0.048}	0.529 _{0.028}	0.630 _{0.066}	0.615 _{0.105}	0.570 _{0.098}	0.575 _{0.095}	0.882 _{0.013}	0.748 _{0.005}	0.771 _{0.013}
	SR-CLAM	0.17	0.638 _{0.053}	0.531 _{0.100}	0.607 _{0.070}	0.628 _{0.074}	0.556 _{0.047}	0.567 _{0.048}	0.909 _{0.024}	0.799 _{0.029}	0.813 _{0.043}
	TransMIL [39]	2.41	0.535 _{0.122}	0.456 _{0.112}	0.615 _{0.009}	0.638 _{0.058}	0.537 _{0.113}	0.565 _{0.079}	0.827 _{0.007}	0.660 _{0.045}	0.665 _{0.040}
	SR-TransMIL	2.01	0.639 _{0.043}	0.563 _{0.037}	0.628 _{0.062}	0.737 _{0.028}	0.545 _{0.018}	0.593 _{0.018}	0.854 _{0.008}	0.708 _{0.017}	0.709 _{0.030}
	CATE [23]	1.93	0.603 _{0.104}	0.536 _{0.133}	0.646 _{0.032}	0.662 _{0.047}	0.552 _{0.072}	0.575 _{0.054}	0.870 _{0.011}	0.690 _{0.021}	0.668 _{0.029}
2	SR-CATE	0.84	0.631 _{0.073}	0.542 _{0.138}	0.638 _{0.020}	0.672 _{0.013}	0.557 _{0.006}	0.583 _{0.004}	0.886 _{0.007}	0.734 _{0.038}	0.742 _{0.036}
	ViLaMIL [40]	40.7	0.624 _{0.056}	0.521 _{0.090}	0.628 _{0.028}	0.889 _{0.020}	0.795 _{0.019}	0.797 _{0.019}	0.952 _{0.008}	0.809 _{0.013}	0.842 _{0.011}
	ABMIL [25]	0.26	0.614 _{0.139}	0.519 _{0.120}	0.607 _{0.062}	0.899 _{0.092}	0.811 _{0.056}	0.812 _{0.055}	0.958 _{0.023}	0.800 _{0.038}	0.838 _{0.042}
	SR-ABMIL	0.18	0.687 _{0.163}	0.584 _{0.182}	0.636 _{0.185}	0.946 _{0.014}	0.855 _{0.024}	0.856 _{0.023}	0.979 _{0.003}	0.851 _{0.013}	0.882 _{0.009}
	CLAM [33]	0.53	0.554 _{0.086}	0.528 _{0.036}	0.607 _{0.047}	0.946 _{0.009}	0.859 _{0.017}	0.859 _{0.017}	0.988 _{0.003}	0.889 _{0.009}	0.907 _{0.017}
	SR-CLAM	0.17	0.682 _{0.053}	0.571 _{0.164}	0.674 _{0.104}	0.951 _{0.002}	0.861 _{0.014}	0.862 _{0.013}	0.989 _{0.003}	0.889 _{0.002}	0.916 _{0.003}
	TransMIL [39]	2.41	0.516 _{0.122}	0.456 _{0.112}	0.615 _{0.009}	0.868 _{0.003}	0.785 _{0.012}	0.786 _{0.012}	0.971 _{0.002}	0.832 _{0.019}	0.869 _{0.016}
	SR-TransMIL	2.01	0.606 _{0.108}	0.467 _{0.059}	0.602 _{0.058}	0.891 _{0.028}	0.796 _{0.018}	0.796 _{0.018}	0.973 _{0.004}	0.850 _{0.002}	0.882 _{0.003}
4	CATE [23]	1.93	0.610 _{0.012}	0.538 _{0.026}	0.615 _{0.043}	0.854 _{0.007}	0.764 _{0.007}	0.764 _{0.007}	0.935 _{0.065}	0.808 _{0.084}	0.823 _{0.107}
	SR-CATE	0.84	0.600 _{0.105}	0.554 _{0.150}	0.646 _{0.038}	0.903 _{0.008}	0.808 _{0.016}	0.809 _{0.016}	0.987 _{0.001}	0.890 _{0.014}	0.916 _{0.012}
	ViLaMIL [40]	40.7	0.562 _{0.130}	0.550 _{0.127}	0.589 _{0.129}	0.903 _{0.019}	0.834 _{0.034}	0.834 _{0.035}	0.960 _{0.016}	0.807 _{0.048}	0.839 _{0.044}
	ABMIL [25]	0.26	0.720 _{0.027}	0.706 _{0.010}	0.760 _{0.022}	0.910 _{0.023}	0.826 _{0.021}	0.826 _{0.021}	0.974 _{0.003}	0.865 _{0.008}	0.893 _{0.009}
	SR-ABMIL	0.18	0.749 _{0.019}	0.720 _{0.011}	0.749 _{0.016}	0.924 _{0.038}	0.855 _{0.050}	0.855 _{0.050}	0.982 _{0.001}	0.889 _{0.017}	0.909 _{0.017}
	CLAM [33]	0.53	0.778 _{0.055}	0.740 _{0.051}	0.762 _{0.050}	0.936 _{0.008}	0.867 _{0.010}	0.867 _{0.010}	0.986 _{0.000}	0.912 _{0.003}	0.929 _{0.005}
	SR-CLAM	0.17	0.801 _{0.032}	0.765 _{0.028}	0.786 _{0.029}	0.946 _{0.006}	0.884 _{0.003}	0.884 _{0.003}	0.988 _{0.000}	0.916 _{0.004}	0.934 _{0.002}
	TransMIL [39]	2.41	0.461 _{0.051}	0.479 _{0.054}	0.548 _{0.045}	0.854 _{0.035}	0.771 _{0.055}	0.774 _{0.052}	0.974 _{0.006}	0.853 _{0.005}	0.880 _{0.004}
8	SR-TransMIL	2.01	0.570 _{0.110}	0.509 _{0.104}	0.550 _{0.116}	0.915 _{0.003}	0.847 _{0.021}	0.847 _{0.022}	0.980 _{0.002}	0.863 _{0.009}	0.895 _{0.002}
	CATE [23]	1.93	0.707 _{0.025}	0.671 _{0.041}	0.698 _{0.051}	0.857 _{0.012}	0.773 _{0.009}	0.774 _{0.008}	0.980 _{0.001}	0.874 _{0.008}	0.896 _{0.011}
	SR-CATE	0.84	0.790 _{0.031}	0.746 _{0.035}	0.773 _{0.037}	0.911 _{0.005}	0.827 _{0.013}	0.828 _{0.012}	0.987 _{0.000}	0.916 _{0.005}	0.934 _{0.002}
	ViLaMIL [40]	40.7	0.787 _{0.024}	0.764 _{0.036}	0.809 _{0.025}	0.940 _{0.007}	0.857 _{0.012}	0.857 _{0.012}	0.976 _{0.011}	0.867 _{0.033}	0.890 _{0.028}
	ABMIL [25]	0.26	0.790 _{0.187}	0.738 _{0.154}	0.760 _{0.161}	0.948 _{0.016}	0.881 _{0.027}	0.881 _{0.027}	0.984 _{0.002}	0.902 _{0.028}	0.919 _{0.023}
	SR-ABMIL	0.18	0.850 _{0.011}	0.796 _{0.012}	0.829 _{0.008}	0.953 _{0.015}	0.896 _{0.016}	0.896 _{0.016}	0.986 _{0.003}	0.923 _{0.011}	0.937 _{0.012}
	CLAM [33]	0.53	0.861 _{0.039}	0.784 _{0.039}	0.798 _{0.049}	0.949 _{0.006}	0.899 _{0.010}	0.899 _{0.010}	0.993 _{0.000}	0.931 _{0.012}	0.945 _{0.011}
	SR-CLAM	0.17	0.858 _{0.021}	0.824 _{0.005}	0.848 _{0.004}	0.950 _{0.010}	0.896 _{0.013}	0.896 _{0.013}	0.994 _{0.002}	0.940 _{0.004}	0.950 _{0.002}
16	TransMIL [39]	2.41	0.539 _{0.070}	0.456 _{0.164}	0.509 _{0.137}	0.932 _{0.003}	0.849 _{0.003}	0.849 _{0.002}	0.984 _{0.003}	0.894 _{0.004}	0.905 _{0.007}
	SR-TransMIL	2.01	0.885 _{0.042}	0.795 _{0.042}	0.817 _{0.044}	0.948 _{0.001}	0.876 _{0.009}	0.876 _{0.009}	0.988 _{0.004}	0.911 _{0.013}	0.923 _{0.009}
	CATE [23]	1.93	0.907 _{0.018}	0.839 _{0.018}	0.855 _{0.020}	0.929 _{0.003}	0.831 _{0.021}	0.833 _{0.020}	0.982 _{0.010}	0.896 _{0.018}	0.920 _{0.011}
	SR-CATE	0.84	0.918 _{0.031}	0.876 _{0.021}	0.886 _{0.020}	0.954 _{0.002}	0.887 _{0.018}	0.887 _{0.018}	0.991 _{0.000}	0.929 _{0.002}	0.943 _{0.002}
	ViLaMIL [40]	40.7	0.858 _{0.052}	0.828 _{0.035}	0.848 _{0.027}	0.960 _{0.006}	0.857 _{0.020}	0.857 _{0.020}	0.988 _{0.004}	0.899 _{0.014}	0.912 _{0.015}
	ABMIL [25]	0.26	0.874 _{0.081}	0.836 _{0.072}	0.850 _{0.072}	0.969 _{0.004}	0.920 _{0.013}	0.920 _{0.013}	0.993 _{0.002}	0.933 _{0.016}	0.943 _{0.015}
	SR-ABMIL	0.18	0.901 _{0.030}	0.860 _{0.050}	0.873 _{0.044}	0.971 _{0.003}	0.920 _{0.010}	0.920 _{0.010}	0.995 _{0.000}	0.932 _{0.008}	0.943 _{0.006}
	CLAM [33]	0.53	0.915 _{0.009}	0.835 _{0.011}	0.856 _{0.012}	0.962 _{0.004}	0.915 _{0.006}	0.915 _{0.006}	0.997 _{0.001}	0.961 _{0.012}	0.963 _{0.005}
TCGA-NSCLC	SR-CLAM	0.17	0.941 _{0.004}	0.876 _{0.021}	0.884 _{0.023}	0.970 _{0.003}	0.920 _{0.011}	0.920 _{0.011}	0.998 _{0.000}	0.960 _{0.007}	0.967 _{0.005}
	TransMIL [39]	2.41	0.868 _{0.079}	0.837 _{0.103}	0.855 _{0.090}	0.952 _{0.004}	0.881 _{0.002}	0.881 _{0.002}	0.983 _{0.008}	0.875 _{0.031}	0.903 _{0.025}
	SR-TransMIL	2.01	0.944 _{0.007}	0.887 _{0.044}	0.899 _{0.034}	0.962 _{0.001}	0.901 _{0.004}	0.901 _{0.004}	0.993 _{0.002}	0.949 _{0.005}	0.952 _{0.002}
	CATE [23]	1.93	0.917 _{0.014}	0.878 _{0.012}	0.889 _{0.009}	0.950 _{0.008}	0.891 _{0.008}	0.891 _{0.008}	0.988 _{0.001}	0.922 _{0.002}	0.933 _{0.007}
	SR-CATE	0.84	0.935 _{0.003}	0.910 _{0.012}	0.917 _{0.012}	0.966 _{0.004}	0.914 _{0.008}	0.914 _{0.008}	0.997 _{0.001}	0.946 _{0.017}	0.954 _{0.014}
	ViLaMIL [40]	40.7	0.858 _{0.052}	0.828 _{0.035}	0.848 _{0.027}	0.960 _{0.006}	0.857 _{0.020}	0.857 _{0.020}	0.988 _{0.004}	0.899 _{0.014}	0.912 _{0.015}
	ABMIL [25]	0.26	0.874 _{0.081}	0.836 _{0.072}	0.850 _{0.072}	0.969 _{0.004}	0.920 _{0.013}	0.920 _{0.013}	0.993 _{0.002}	0.933 _{0.016}	0.943 _{0.015}
	SR-ABMIL	0.18	0.901 _{0.030}	0.860 _{0.050}	0.873 _{0.044}	0.971 _{0.003}	0.920 _{0.010}	0.920 _{0.010}	0.995 _{0.000}	0.932 _{0.008}	0.943 _{0.006}

4 Experiments and Results

4.1 Dataset Descriptions

We conduct extensive experiments on Camelyon16 [30], TCGA-NSCLC and TCGA-RCC datasets. The details of the datasets used in this work are available in Appendix D.1.

4.2 Implementation Details

Evaluation Metrics. We employ three complementary metrics for comprehensive assessment: Area Under the Receiver Operating Characteristic Curve (AUC), F1-score, and accuracy.

Experimental Protocol. We benchmark our approach on established multiple instance learning frameworks: AB-MIL [25] (attention-based method), CLAM [33] (attention-based method with patch classification constraint), TransMIL [39] (Transformer-based method), CATE [23] (information-theory-based method). In addition, we also compare our methods with ViLaMIL [40], a recent visual language model specifically proposed for few-shot WSI classification. All implementations utilize

Table 2: Ablation studies of our proposed method across varying shot settings on the Camelyon16, TCGA-NSCLC, and TCGA-RCC datasets. Metrics highlighted in bold red indicate the top result, while those in italicized blue denote the second-best result.

#S	Methods	#P	Camelyon16			TCGA-NSCLC			TCGA-RCC		
			AUC \uparrow	F1 \uparrow	Acc. \uparrow	AUC \uparrow	F1 \uparrow	Acc. \uparrow	AUC \uparrow	F1 \uparrow	Acc. \uparrow
8	Ours	0.17	0.858 _{0.021}	0.824 _{0.005}	0.848 _{0.004}	0.950 _{0.010}	0.896 _{0.013}	0.896 _{0.013}	0.994 _{0.002}	0.940 _{0.004}	0.950 _{0.002}
	- SP	0.01	0.595 _{0.017}	0.439 _{0.098}	0.633 _{0.022}	0.906 _{0.013}	0.826 _{0.019}	0.826 _{0.019}	0.974 _{0.003}	0.892 _{0.021}	0.902 _{0.013}
	- Random	0.17	0.525 _{0.111}	0.275 _{0.000}	0.380 _{0.000}	0.328 _{0.032}	0.343 _{0.015}	0.401 _{0.012}	0.613 _{0.191}	0.204 _{0.101}	0.309 _{0.154}
	- GELU	0.17	0.822 _{0.029}	0.793 _{0.038}	0.822 _{0.031}	0.951 _{0.007}	0.902 _{0.006}	0.902 _{0.006}	0.988 _{0.001}	0.939 _{0.001}	0.950 _{0.002}
	ReLU	0.17	0.840 _{0.031}	0.823 _{0.032}	0.845 _{0.027}	0.955 _{0.002}	0.906 _{0.008}	0.906 _{0.008}	0.992 _{0.001}	0.939 _{0.005}	0.948 _{0.005}
	Sigmoid	0.17	0.810 _{0.021}	0.719 _{0.079}	0.729 _{0.084}	0.947 _{0.001}	0.905 _{0.010}	0.905 _{0.010}	0.990 _{0.000}	0.883 _{0.022}	0.910 _{0.017}
	Tanh	0.17	0.789 _{0.020}	0.752 _{0.089}	0.767 _{0.097}	0.950 _{0.004}	0.900 _{0.004}	0.900 _{0.004}	0.990 _{0.003}	0.934 _{0.004}	0.943 _{0.005}
16	Ours	0.17	0.941 _{0.004}	0.876 _{0.021}	0.884 _{0.023}	0.970 _{0.003}	0.920 _{0.011}	0.920 _{0.011}	0.998 _{0.000}	0.960 _{0.007}	0.967 _{0.005}
	- SP	0.01	0.561 _{0.018}	0.550 _{0.013}	0.656 _{0.022}	0.938 _{0.013}	0.883 _{0.019}	0.883 _{0.019}	0.986 _{0.001}	0.897 _{0.015}	0.919 _{0.011}
	- Random	0.17	0.525 _{0.111}	0.274 _{0.002}	0.377 _{0.004}	0.328 _{0.032}	0.345 _{0.016}	0.384 _{0.017}	0.614 _{0.191}	0.213 _{0.099}	0.311 _{0.154}
	- GELU	0.17	0.938 _{0.013}	0.872 _{0.005}	0.876 _{0.004}	0.967 _{0.002}	0.918 _{0.014}	0.918 _{0.014}	0.997 _{0.000}	0.950 _{0.011}	0.959 _{0.007}
	ReLU	0.17	0.939 _{0.003}	0.887 _{0.023}	0.894 _{0.024}	0.968 _{0.003}	0.916 _{0.014}	0.916 _{0.014}	0.997 _{0.000}	0.959 _{0.011}	0.966 _{0.009}
	Sigmoid	0.17	0.778 _{0.061}	0.698 _{0.075}	0.713 _{0.084}	0.956 _{0.004}	0.905 _{0.012}	0.905 _{0.012}	0.988 _{0.006}	0.919 _{0.022}	0.922 _{0.015}
	Tanh	0.17	0.806 _{0.032}	0.568 _{0.145}	0.584 _{0.126}	0.615 _{0.105}	0.570 _{0.098}	0.575 _{0.095}	0.882 _{0.013}	0.748 _{0.005}	0.771 _{0.013}

Table 3: Performance of ABMIL with replaced linear layers under varying shot settings on Camelyon16, TCGA-NSCLC, and TCGA-RCC datasets. “U” and “V” denote two matrices in ABMIL.

#S	Methods	#P	Camelyon16			TCGA-NSCLC			TCGA-RCC		
			AUC \uparrow	F1 \uparrow	Acc. \uparrow	AUC \uparrow	F1 \uparrow	Acc. \uparrow	AUC \uparrow	F1 \uparrow	Acc. \uparrow
8	V	0.18	0.850 _{0.011}	0.796 _{0.012}	0.829 _{0.008}	0.953 _{0.015}	0.896 _{0.016}	0.896 _{0.016}	0.986 _{0.003}	0.923 _{0.011}	0.937 _{0.012}
	U	0.18	0.837 _{0.038}	0.776 _{0.046}	0.814 _{0.034}	0.924 _{0.039}	0.855 _{0.060}	0.856 _{0.059}	0.961 _{0.030}	0.853 _{0.035}	0.873 _{0.037}
	V + U	0.10	0.846 _{0.025}	0.797 _{0.028}	0.829 _{0.021}	0.948 _{0.007}	0.892 _{0.029}	0.892 _{0.029}	0.988 _{0.002}	0.926 _{0.003}	0.939 _{0.002}
16	V	0.18	0.901 _{0.030}	0.860 _{0.050}	0.873 _{0.044}	0.971 _{0.003}	0.920 _{0.010}	0.920 _{0.010}	0.995 _{0.000}	0.932 _{0.008}	0.943 _{0.006}
	U	0.18	0.919 _{0.029}	0.888 _{0.031}	0.899 _{0.027}	0.963 _{0.003}	0.919 _{0.010}	0.919 _{0.010}	0.989 _{0.004}	0.913 _{0.011}	0.934 _{0.010}
	V + U	0.10	0.879 _{0.020}	0.826 _{0.005}	0.837 _{0.008}	0.971 _{0.002}	0.925 _{0.002}	0.925 _{0.002}	0.996 _{0.001}	0.950 _{0.002}	0.954 _{0.002}

their official codes. We employ early stopping with a patience of 20 epochs on validation loss, while enforcing a minimum training duration of 50 epochs. To mitigate initialization bias, we conduct three training runs for each method and report the mean performances with standard deviations.

Hyper-parameters Details. We use the AdamW [31] optimizer in all of our experiments. We set the learning rate and weight decay to be 5×10^{-4} and 10^{-5} . The linear scheduler is utilized for our methods with starting factor and end factor being 0.01 and 0.1, respectively. Dropout is set to 0.25. The batch size is set to 1 throughout the experiments. All methods utilized the same random seeds. We use CONCH [32], UNI [4] and ResNet-50 [17] to extract features from the non-overlapping 224×224 patches, obtained from $20 \times$ magnification of the WSIs, and the resulting feature dimensions are 512, 1,024 and 1,024, respectively. The rank r is set to 64. GELU [19] activation function is chosen for our SR block as it demonstrates the most superior performance among others.

4.3 Comparison with State-of-the-art Methods

Table 1 presents the results of few-shot ($k = 1, 2, 4, 8, 16$) setting on Camelyon16, TCGA-NSCLC, and TCGA-RCC. Three significant findings emerge from this analysis. First, our method (denoted by the “SR-” prefix) demonstrates superior performance compared to both baseline architectures and the current state-of-the-art, ViLaMIL [40], despite the latter utilizing 226 times more trainable parameters than SR-ABMIL. Second, our approach yields improvements in F1 scores and accuracy compared to baseline models, even when AUC enhancements appear modest. For instance, at $k = 16$, SR-TransMIL exhibits 7.4% and 4.9% improvements in F1 and accuracy on the TCGA-RCC dataset despite 1% gains in AUC score. Third, we observe that task complexity influences optimal model architecture: more challenging tasks (*e.g.*, Camelyon16) benefit from sophisticatedly designed models, while tasks with distinctive morphological patterns (*e.g.*, TCGA-RCC) achieve better results with simpler architectures. These findings demonstrate our method enhances class discrimination and creates more robust decision boundaries across varying task complexities in few-shot learning.

Camelyon16 presents unique challenges, evidenced by lower performance metrics. This task appears particularly difficult in extreme settings, with most models struggling to exceed 0.60 F1 scores at

Table 4: Experimental results on different initialization methods in TransMIL under various shot settings across Camelyon16, TCGA-NSCLC and TCGA-RCC dataset. “K.” stands for Kaiming initialization, “X” stands for Xavier initialization, “U.” stands for uniform distribution, and the number following is the input parameter for initialization.

k	Methods	Camelyon16			TCGA-NSCLC			TCGA-RCC		
		AUC \uparrow	F1 \uparrow	Acc. \uparrow	AUC \uparrow	F1 \uparrow	Acc. \uparrow	AUC \uparrow	F1 \uparrow	Acc. \uparrow
8	K. U. $\sqrt{5}$	0.885 _{0.042}	0.795 _{0.042}	0.817 _{0.044}	0.948 _{0.001}	0.876 _{0.009}	0.876 _{0.009}	0.988 _{0.004}	0.911 _{0.013}	0.923 _{0.009}
	K. U. 0	0.623 _{0.165}	0.564 _{0.140}	0.571 _{0.150}	0.926 _{0.003}	0.848 _{0.021}	0.848 _{0.021}	0.821 _{0.278}	0.679 _{0.382}	0.791 _{0.204}
	K. N. 0	0.670 _{0.124}	0.597 _{0.163}	0.605 _{0.175}	0.644 _{0.249}	0.512 _{0.310}	0.624 _{0.214}	0.660 _{0.278}	0.449 _{0.364}	0.664 _{0.188}
	X. U. 1	0.730 _{0.135}	0.687 _{0.160}	0.705 _{0.175}	0.931 _{0.013}	0.860 _{0.018}	0.861 _{0.018}	0.816 _{0.274}	0.683 _{0.385}	0.796 _{0.209}
	X. N. 1	0.559 _{0.046}	0.498 _{0.065}	0.504 _{0.061}	0.939 _{0.021}	0.879 _{0.029}	0.880 _{0.029}	0.822 _{0.279}	0.678 _{0.381}	0.791 _{0.204}
16	K. U. $\sqrt{5}$	0.944 _{0.007}	0.887 _{0.044}	0.899 _{0.034}	0.962 _{0.001}	0.901 _{0.004}	0.901 _{0.004}	0.993 _{0.002}	0.949 _{0.005}	0.952 _{0.002}
	K. U. 0	0.901 _{0.063}	0.873 _{0.067}	0.881 _{0.063}	0.652 _{0.263}	0.525 _{0.322}	0.641 _{0.222}	0.986 _{0.007}	0.900 _{0.016}	0.920 _{0.015}
	K. N. 0	0.916 _{0.053}	0.841 _{0.040}	0.855 _{0.031}	0.486 _{0.025}	0.339 _{0.000}	0.513 _{0.000}	0.663 _{0.282}	0.460 _{0.385}	0.676 _{0.210}
	X. U. 1	0.933 _{0.030}	0.868 _{0.027}	0.879 _{0.027}	0.804 _{0.263}	0.713 _{0.323}	0.771 _{0.223}	0.656 _{0.289}	0.443 _{0.423}	0.605 _{0.317}
	X. N. 1	0.930 _{0.045}	0.873 _{0.051}	0.884 _{0.048}	0.956 _{0.004}	0.900 _{0.006}	0.900 _{0.006}	0.919 _{0.123}	0.684 _{0.386}	0.801 _{0.212}

Table 5: Experimental results on different pretrained feature extractors under various shot settings. “R” stands for ResNet50, “U” stands for UNI, and “L” stands for MIL model with our method.

k	E.	TCGA-NSCLC						TCGA-RCC					
		AUC \uparrow	ABMIL F1 \uparrow	Acc. \uparrow	AUC \uparrow	TransMIL F1 \uparrow	Acc. \uparrow	AUC \uparrow	ABMIL F1 \uparrow	Acc. \uparrow	AUC \uparrow	TransMIL F1 \uparrow	Acc. \uparrow
8	R	0.666 _{0.037}	0.627 _{0.016}	0.627 _{0.017}	0.692 _{0.054}	0.504 _{0.127}	0.574 _{0.061}	0.839 _{0.018}	0.686 _{0.038}	0.709 _{0.049}	0.868 _{0.055}	0.607 _{0.072}	0.681 _{0.051}
	RL	0.710 _{0.006}	0.668 _{0.009}	0.668 _{0.009}	0.667 _{0.095}	0.523 _{0.116}	0.569 _{0.071}	0.851 _{0.003}	0.699 _{0.019}	0.726 _{0.020}	0.917 _{0.007}	0.743 _{0.019}	0.768 _{0.009}
	U	0.814 _{0.070}	0.746 _{0.076}	0.747 _{0.076}	0.842 _{0.011}	0.761 _{0.006}	0.762 _{0.006}	0.984 _{0.008}	0.901 _{0.053}	0.909 _{0.052}	0.983 _{0.003}	0.890 _{0.017}	0.899 _{0.020}
	UL	0.910 _{0.028}	0.836 _{0.027}	0.837 _{0.027}	0.859 _{0.026}	0.779 _{0.014}	0.779 _{0.014}	0.989 _{0.001}	0.919 _{0.010}	0.927 _{0.004}	0.985 _{0.001}	0.897 _{0.010}	0.902 _{0.007}
16	R	0.618 _{0.037}	0.577 _{0.016}	0.580 _{0.017}	0.590 _{0.027}	0.483 _{0.077}	0.540 _{0.029}	0.745 _{0.072}	0.570 _{0.125}	0.564 _{0.133}	0.752 _{0.055}	0.533 _{0.049}	0.577 _{0.069}
	RL	0.666 _{0.006}	0.635 _{0.010}	0.635 _{0.010}	0.585 _{0.011}	0.538 _{0.054}	0.556 _{0.028}	0.814 _{0.045}	0.629 _{0.046}	0.625 _{0.049}	0.873 _{0.045}	0.696 _{0.075}	0.711 _{0.091}
	U	0.891 _{0.040}	0.843 _{0.031}	0.843 _{0.031}	0.892 _{0.042}	0.814 _{0.037}	0.815 _{0.038}	0.993 _{0.001}	0.948 _{0.011}	0.953 _{0.013}	0.994 _{0.001}	0.945 _{0.013}	0.950 _{0.016}
	UL	0.945 _{0.005}	0.891 _{0.015}	0.891 _{0.014}	0.907 _{0.017}	0.842 _{0.022}	0.843 _{0.021}	0.995 _{0.002}	0.948 _{0.008}	0.954 _{0.005}	0.995 _{0.001}	0.944 _{0.004}	0.949 _{0.007}

$k = 1$ and $k = 2$. Our approach demonstrates dramatic improvements, with SR-TransMIL achieving a 34.6% absolute gain in AUC score over TransMIL at $k = 8$ (0.539 vs. 0.885). The performance trajectory from $k = 1$ to $k = 16$ is notably steep, with our methods showing increasingly dominant performance as k increases. This suggests that our method is effective at extracting meaningful features from limited samples, where visual patterns may be more subtle and complex.

TCGA-NSCLC dataset reveals a distinctive pattern where lightweight models such as SR-CLAM and SR-ABMIL consistently achieve the highest performance, in contrast to Camelyon16 where more complex models tend to excel at higher shot counts. This lung cancer classification task appears more amenable to few-shot learning than Camelyon16, with baseline performances starting much higher and exceeding 0.90 AUC for multiple models when $k \geq 4$. Our method shows consistent improvements across all architectures, though the magnitude varies among model architectures. Notably, SR-CLAM achieves exceptional AUC scores while utilizing only 0.17M parameters, demonstrating that architectural efficiency rather than parameter count may be the determining factor for this dataset.

TCGA-RCC dataset reveals the highest overall performance among all datasets, indicating this task may present more distinct morphological patterns. Even at $k = 1$, several models achieve AUC values exceeding 0.85, and by $k = 16$, all models reach near-perfect discrimination with AUC values above 0.99. A unique characteristic of this dataset is the smaller gap between AUC and F1/accuracy metrics, suggesting clearer decision boundaries. SR-CLAM demonstrates particularly impressive results, outperforming all other approaches regardless of trainable parameter count. The substantial gains in accuracy metrics even when AUC improvements are marginal (SR-TransMIL at $k = 16$) indicate that our method effectively optimizes decision thresholds. We also notice that for this dataset, simpler architectures may be preferable to more complex models with larger parameter counts.

4.4 Ablation Studies and Sensitivity Analysis

Recalibration matrix and SP. We conducted ablation studies on two components of our method: the randomly initialized frozen matrix B and the SP. As evidenced in Tables 2 and 6, our complete method consistently demonstrates superior performance. A notable experimental finding reveals that

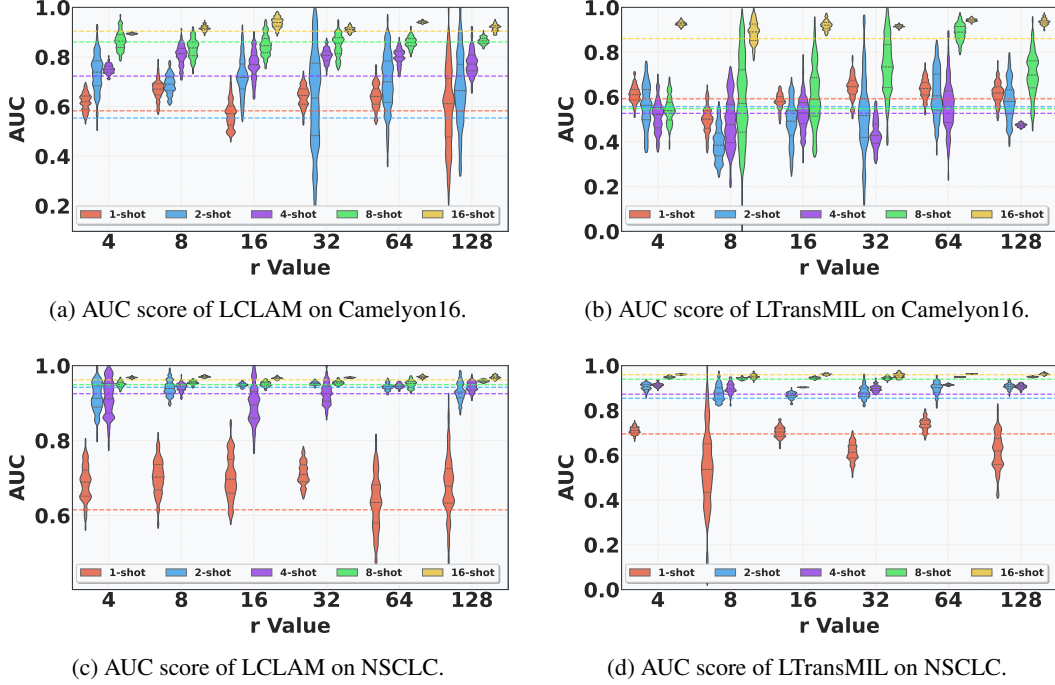


Figure 2: Sensitivity analysis of parameter r across multiple datasets using LCLAM and LTransMIL. Dashed lines indicate the performance of the respective baseline methods (CLAM and TransMIL).

when the random recalibration matrix B is eliminated while maintaining SP, performance degrades significantly, resulting in severe model impairment. This empirical evidence strongly suggests that the random recalibration matrix B serves a more essential function than SP, highlighting its crucial role in facilitating effective residual learning and feature enrichment.

Position-dependent Performance Analysis. We conduct a layer-wise ablation study to evaluate how our method affects performance when implemented at different positions within MIL. We selected ABMIL [25] due to its structural simplicity, with results reported in Tables 3 and 7. This study investigates the two components of ABMIL [25], U and V , analyzing performances when selectively replacing these components with the SR block. The results demonstrate that optimal performance is achieved when both components are replaced with our SR block, while replacing only the V component yields the second-best performance. These validate the position robustness of our method.

Choice of Activation Function. We evaluated the efficacy of various activation functions, including a baseline without any activation function, with quantitative results presented in Tables 2 and 6. The observed performance gaps between our method and its variants lacking activation functions provide empirical validation of our theoretical framework, confirming that the non-linear formulation constitutes a substantial enhancement over the linear case. In the context of activation function selection, our experiments indicate that while GELU activation delivers optimal overall performance, the ReLU function exhibits comparable effectiveness, occasionally outperforming GELU activation.

Choice of Initialization Method. Given the diversity of initialization techniques, we conducted a study to determine the optimal initialization strategy. Our evaluation includes the most widely adopted methods: Kaiming uniform/normal and Xavier uniform/normal distributions. The results are presented in Tables 4 and 8. These findings demonstrate significant performance degradation when employing normal distribution-based initializations, regardless of whether Kaiming or Xavier variants were implemented, likely attributed to larger variance of the normal distribution. Additionally, uniform distribution methods with $\text{gain} = 0$ underperforms the default method ($\text{gain} = \sqrt{5}$), which can be attributed to different initialization between the SR block and rest of the MIL model.

Foundation Model Selection. We investigated which foundation model yields optimal performance and whether our approach demonstrates compatibility across different embeddings. Using CONCH, UNI, and ResNet50 with TransMIL and ABMIL, we present results in Tables 5 and 9. CONCH

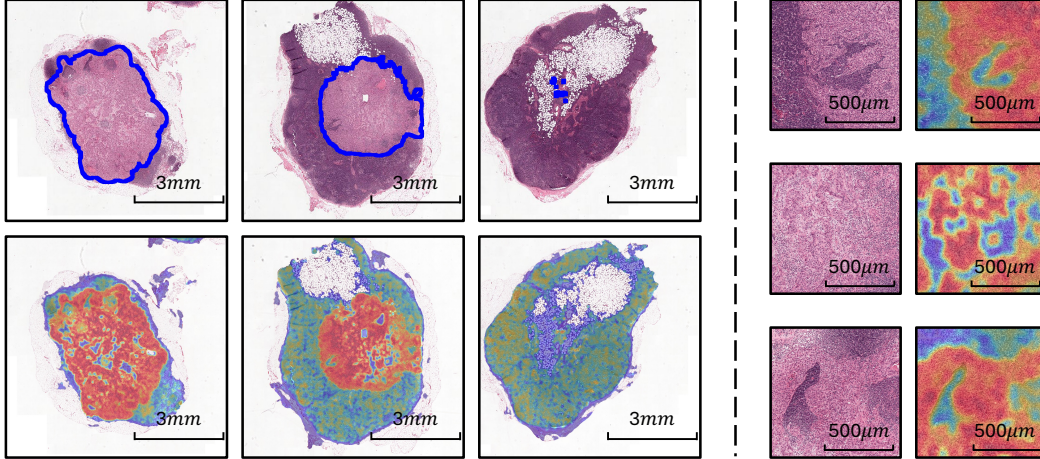


Figure 3: SR-CLAM-generated heatmaps for tumor049 (Camelyon16). The left panel shows heatmaps for three biopsy regions, while the right panel displays fine-grained patches with their heatmaps. Red indicates high attention (tumor), whereas blue indicates low attention (normal tissue).

embeddings consistently outperformed UNI and ResNet50, aligning with expectations as ResNet50 lacks pathology pretraining. The dimensional difference between UNI (1,024) and CONCH (512) likely contributes to lower performance of UNI due to inflated higher-dimensional spaces under few-shot settings. Our method demonstrated consistent improvements over baselines across all model combinations, substantiating its robustness across diverse MIL and foundation models.

Sensitivity Analysis of the Rank. The rank r plays a critical role in our method, as it simultaneously governs the number of trainable parameters and constrains the information flow through the low-rank bottleneck. As illustrated in Figs. 2 and 4, when $r = 64$, the model achieves an optimal balance between performance metrics and their associated standard deviations. Notably, our experiments reveal an intriguing phenomenon at $r = 4$, where the model demonstrates exceptional robustness despite the severe dimensionality constraint. It not only attains competitive performance with low variance, but in certain evaluation scenarios, it surpasses configurations with higher rank values ($r = 8, 16$). This counter-intuitive finding suggests that extremely low-rank projections may capture essential task-relevant information while effectively filtering out noise signals in the feature space.

4.5 Model Interpretability Analysis

Figure 3 illustrates the heatmaps generated by our SR-CLAM compared with the ground truth labels. Tumor049 from the Camelyon16 [30] is presented as an example. In the original images (upper left), blue curves delineate the approximate tumor boundaries, and the corresponding heatmap is shown in the lower left panel. Notably, our method captures additional fine-grained boundaries not indicated in the original annotations, as shown in the right panel. Although all regions on the right fall within the blue-delineated tumor boundaries, our model precisely identifies the boundaries between distinct morphological patterns, demonstrating its sensitivity in capturing tumor heterogeneity.

5 Conclusion

In this work, we showed that our SR block effectively mitigates overfitting and suppresses the learning of spurious features, while eliminating the complex preprocessing and excessive parameter overhead of recent VLMs. These are achieved through an elegant yet simple design: combining a trainable SP with a frozen recalibration matrix. Extensive experimental results confirms that our SR block serves as an effective drop-in replacement for linear layers in mainstream MIL models, consistently enhancing their performance under few-shot constraints. Given its minimal implementation requirements, strong empirical results, and theoretical guarantees, we expect the SR block to be broadly applicable across diverse few-shot learning tasks and architectures. Future work will explore its adaptation to other domains beyond computational pathology, such as natural images and natural language processing.

References

- [1] Andrew R Barron. Universal approximation bounds for superpositions of a sigmoidal function. *IEEE Transactions on Information theory*, 39(3):930–945, 1993.
- [2] Gabriele Campanella, Matthew G Hanna, Luke Geneslaw, Allen Miraflor, Vitor Werneck Krauss Silva, Klaus J Busam, Edi Brogi, Victor E Reuter, David S Klimstra, and Thomas J Fuchs. Clinical-grade computational pathology using weakly supervised deep learning on whole slide images. *Nature medicine*, 25(8):1301–1309, 2019.
- [3] Kaitao Chen, Shiliang Sun, and Jing Zhao. Camil: Causal multiple instance learning for whole slide image classification. In *Proceedings of the AAAI Conference on Artificial Intelligence*, volume 38, pages 1120–1128, 2024.
- [4] Richard J Chen, Tong Ding, Ming Y Lu, Drew FK Williamson, Guillaume Jaume, Bowen Chen, Andrew Zhang, Daniel Shao, Andrew H Song, Muhammad Shaban, et al. Towards a general-purpose foundation model for computational pathology. *Nature Medicine*, 2024.
- [5] Philip Chikontwe, Meejeong Kim, Soo Jeong Nam, Heounjeong Go, and Sang Hyun Park. Multiple instance learning with center embeddings for histopathology classification. In *Medical Image Computing and Computer Assisted Intervention–MICCAI 2020: 23rd International Conference, Lima, Peru, October 4–8, 2020, Proceedings, Part V 23*, pages 519–528. Springer, 2020.
- [6] George Cybenko. Approximation by superpositions of a sigmoidal function. *Mathematics of control, signals and systems*, 2(4):303–314, 1989.
- [7] Jia Deng, Wei Dong, Richard Socher, Li-Jia Li, Kai Li, and Li Fei-Fei. Imagenet: A large-scale hierarchical image database. In *2009 IEEE conference on computer vision and pattern recognition*, pages 248–255. Ieee, 2009.
- [8] Yoav Freund and Robert E Schapire. A decision-theoretic generalization of on-line learning and an application to boosting. *Journal of computer and system sciences*, 55(1):119–139, 1997.
- [9] Jerome H Friedman. Greedy function approximation: a gradient boosting machine. *Annals of statistics*, pages 1189–1232, 2001.
- [10] Jerome H Friedman. Stochastic gradient boosting. *Computational statistics & data analysis*, 38(4):367–378, 2002.
- [11] Kexue Fu, Linhao Qu, Shuo Wang, Ying Xiong, Ilias Maglogiannis, Longxiang Gao, Manning Wang, et al. Fast: A dual-tier few-shot learning paradigm for whole slide image classification. *Advances in Neural Information Processing Systems*, 37:105090–105113, 2024.
- [12] Ken-Ichi Funahashi. On the approximate realization of continuous mappings by neural networks. *Neural networks*, 2(3):183–192, 1989.
- [13] Zhengrui Guo, Jiabo Ma, Yingxue Xu, Yihui Wang, Liansheng Wang, and Hao Chen. Histgen: Histopathology report generation via local-global feature encoding and cross-modal context interaction. In *International Conference on Medical Image Computing and Computer-Assisted Intervention*, pages 189–199. Springer, 2024.
- [14] Zhengrui Guo, Qichen Sun, Jiabo Ma, Lishuang Feng, Jinzhuo Wang, and Hao Chen. Context matters: Query-aware dynamic long sequence modeling of gigapixel images. *arXiv preprint arXiv:2501.18984*, 2025.
- [15] Zhengrui Guo, Conghao Xiong, Jiabo Ma, Qichen Sun, Lishuang Feng, Jinzhuo Wang, and Hao Chen. Focus: Knowledge-enhanced adaptive visual compression for few-shot whole slide image classification. In *Proceedings of the IEEE/CVF Conference on Computer Vision and Pattern Recognition (CVPR)*, June 2025.
- [16] Kaiming He, Xiangyu Zhang, Shaoqing Ren, and Jian Sun. Delving deep into rectifiers: Surpassing human-level performance on imagenet classification. In *Proceedings of the IEEE international conference on computer vision*, pages 1026–1034, 2015.

- [17] Kaiming He, Xiangyu Zhang, Shaoqing Ren, and Jian Sun. Deep residual learning for image recognition. In *Proceedings of the IEEE conference on computer vision and pattern recognition*, pages 770–778, 2016.
- [18] Zhiyuan He, Danchen Lin, Thomas Lau, and Mike Wu. Gradient boosting machine: a survey. *arXiv preprint arXiv:1908.06951*, 2019.
- [19] Dan Hendrycks and Kevin Gimpel. Gaussian error linear units (gelus). *arXiv preprint arXiv:1606.08415*, 2016.
- [20] Kurt Hornik, Maxwell Stinchcombe, and Halbert White. Multilayer feedforward networks are universal approximators. *Neural networks*, 2(5):359–366, 1989.
- [21] Le Hou, Dimitris Samaras, Tahsin M Kurc, Yi Gao, James E Davis, and Joel H Saltz. Patch-based convolutional neural network for whole slide tissue image classification. In *Proceedings of the IEEE conference on computer vision and pattern recognition*, pages 2424–2433, 2016.
- [22] Guang-Bin Huang, Qin-Yu Zhu, and Chee-Kheong Siew. Extreme learning machine: theory and applications. *Neurocomputing*, 70(1-3):489–501, 2006.
- [23] Yanyan Huang, Weiqin Zhao, Yihang Chen, Yu Fu, and Lequan Yu. Free lunch in pathology foundation model: Task-specific model adaptation with concept-guided feature enhancement. In *The Thirty-eighth Annual Conference on Neural Information Processing Systems*, 2024.
- [24] Zhi Huang, Federico Bianchi, Mert Yuksekogun, Thomas J Montine, and James Zou. A visual-language foundation model for pathology image analysis using medical twitter. *Nature medicine*, 29(9):2307–2316, 2023.
- [25] Maximilian Ilse, Jakub Tomczak, and Max Welling. Attention-based deep multiple instance learning. In *International conference on machine learning*, pages 2127–2136. PMLR, 2018.
- [26] Fahdi Kanavati, Gouji Toyokawa, Seiya Momosaki, Michael Rambeau, Yuka Kozuma, Fumihiro Shoji, Koji Yamazaki, Sadanori Takeo, Osamu Iizuka, and Masayuki Tsuneki. Weakly-supervised learning for lung carcinoma classification using deep learning. *Scientific reports*, 10(1):9297, 2020.
- [27] Hao Li, Ying Chen, Yifei Chen, Rongshan Yu, Wenxian Yang, Liansheng Wang, Bowen Ding, and Yuchen Han. Generalizable whole slide image classification with fine-grained visual-semantic interaction. In *Proceedings of the IEEE/CVF Conference on Computer Vision and Pattern Recognition*, pages 11398–11407, 2024.
- [28] Jiawen Li, Yuxuan Chen, Hongbo Chu, Qiehe Sun, Tian Guan, Anjia Han, and Yonghong He. Dynamic graph representation with knowledge-aware attention for histopathology whole slide image analysis. In *Proceedings of the IEEE/CVF Conference on Computer Vision and Pattern Recognition*, pages 11323–11332, 2024.
- [29] Tiancheng Lin, Zhimiao Yu, Hongyu Hu, Yi Xu, and Chang-Wen Chen. Interventional bag multi-instance learning on whole-slide pathological images. In *Proceedings of the IEEE/CVF Conference on Computer Vision and Pattern Recognition*, pages 19830–19839, 2023.
- [30] Geert Litjens, Peter Bandi, Babak Ehteshami Bejnordi, Oscar Geessink, Maschenka Balkenhol, Peter Bult, Altuna Halilovic, Meyke Hermesen, Rob van de Loo, Rob Vogels, Quirine F Manson, Nikolas Stathonikos, Alexi Baidoshvili, Paul van Diest, Carla Wauters, Marcory van Dijk, and Jeroen van der Laak. 1399 H&E-stained sentinel lymph node sections of breast cancer patients: the CAMELYON dataset. *GigaScience*, 7(6), June 2018.
- [31] Ilya Loshchilov and Frank Hutter. Decoupled weight decay regularization. In *International Conference on Learning Representations*, 2019.
- [32] Ming Y Lu, Bowen Chen, Drew FK Williamson, Richard J Chen, Ivy Liang, Tong Ding, Guillaume Jaume, Igor Odintsov, Long Phi Le, Georg Gerber, et al. A visual-language foundation model for computational pathology. *Nature Medicine*, 30:863–874, 2024.

- [33] Ming Y Lu, Drew FK Williamson, Tiffany Y Chen, Richard J Chen, Matteo Barbieri, and Faisal Mahmood. Data-efficient and weakly supervised computational pathology on whole-slide images. *Nature biomedical engineering*, 5(6):555–570, 2021.
- [34] Yulong Lu and Jianfeng Lu. A universal approximation theorem of deep neural networks for expressing probability distributions. *Advances in neural information processing systems*, 33:3094–3105, 2020.
- [35] Jiabo Ma, Zhengrui Guo, Fengtao Zhou, Yihui Wang, Yingxue Xu, Yu Cai, Zhengjie Zhu, Cheng Jin, Yi Lin, Xinrui Jiang, et al. Towards a generalizable pathology foundation model via unified knowledge distillation. *arXiv preprint arXiv:2407.18449*, 2024.
- [36] Linhao Qu, Kexue Fu, Manning Wang, Zhijian Song, et al. The rise of ai language pathologists: Exploring two-level prompt learning for few-shot weakly-supervised whole slide image classification. *Advances in Neural Information Processing Systems*, 36:67551–67564, 2023.
- [37] Linhao Qu, Dingkang Yang, Dan Huang, Qin hao Guo, Rongkui Luo, Shaoting Zhang, and Xiaosong Wang. Pathology-knowledge enhanced multi-instance prompt learning for few-shot whole slide image classification. In *European Conference on Computer Vision*, pages 196–212. Springer, 2024.
- [38] Ali Rahimi and Benjamin Recht. Weighted sums of random kitchen sinks: Replacing minimization with randomization in learning. *Advances in neural information processing systems*, 21, 2008.
- [39] Zhuchen Shao, Hao Bian, Yang Chen, Yifeng Wang, Jian Zhang, Xiangyang Ji, et al. Transmil: Transformer based correlated multiple instance learning for whole slide image classification. *Advances in Neural Information Processing Systems*, 34:2136–2147, 2021.
- [40] Jiangbo Shi, Chen Li, Tieliang Gong, Yefeng Zheng, and Huazhu Fu. Vila-mil: Dual-scale vision-language multiple instance learning for whole slide image classification. In *Proceedings of the IEEE/CVF Conference on Computer Vision and Pattern Recognition*, pages 11248–11258, 2024.
- [41] Andrew H. Song, Richard J. Chen, Guillaume Jaume, Anurag Jayant Vaidya, Alexander Baras, and Faisal Mahmood. Multimodal prototyping for cancer survival prediction. In Ruslan Salakhutdinov, Zico Kolter, Katherine Heller, Adrian Weller, Nuria Oliver, Jonathan Scarlett, and Felix Berkenkamp, editors, *Proceedings of the 41st International Conference on Machine Learning*, volume 235 of *Proceedings of Machine Learning Research*, pages 46050–46073. PMLR, 21–27 Jul 2024.
- [42] Yisheng Song, Ting Wang, Puyu Cai, Subrota K Mondal, and Jyoti Prakash Sahoo. A comprehensive survey of few-shot learning: Evolution, applications, challenges, and opportunities. *ACM Computing Surveys*, 55(13s):1–40, 2023.
- [43] Wenhao Tang, Fengtao Zhou, Sheng Huang, Xiang Zhu, Yi Zhang, and Bo Liu. Feature re-embedding: Towards foundation model-level performance in computational pathology. In *Proceedings of the IEEE/CVF Conference on Computer Vision and Pattern Recognition*, pages 11343–11352, 2024.
- [44] Georgios Tsoumplekas, Vladislav Li, Panagiotis Sarigiannidis, and Vasileios Argyriou. A complete survey on contemporary methods, emerging paradigms and hybrid approaches for few-shot learning. *arXiv preprint arXiv:2402.03017*, 2024.
- [45] Eugene Vorontsov, Alican Bozkurt, Adam Casson, George Shaikovski, Michal Zelechowski, Kristen Severson, Eric Zimmermann, James Hall, Neil Tenenholtz, Nicolo Fusi, et al. A foundation model for clinical-grade computational pathology and rare cancers detection. *Nature medicine*, 30(10):2924–2935, 2024.
- [46] Jinxi Xiang, Xiyue Wang, Xiaoming Zhang, Yinghua Xi, Feyisope Eweje, Yijiang Chen, Yuchen Li, Colin Bergstrom, Matthew Gopaulchan, Ted Kim, et al. A vision-language foundation model for precision oncology. *Nature*, pages 1–10, 2025.

- [47] Conghao Xiong, Hao Chen, and Joseph J. Y. Sung. A survey of pathology foundation model: Progress and future directions. *arXiv preprint arXiv:2504.04045*, 2025.
- [48] Conghao Xiong, Hao Chen, Joseph J. Y. Sung, and Irwin King. Diagnose like a pathologist: Transformer-enabled hierarchical attention-guided multiple instance learning for whole slide image classification. In *Proceedings of the Thirty-Second International Joint Conference on Artificial Intelligence, IJCAI-23*, pages 1587–1595, 8 2023. Main Track.
- [49] Conghao Xiong, Hao Chen, Hao Zheng, Dong Wei, Yefeng Zheng, Joseph J. Y. Sung, and Irwin King. Mome: Mixture of multimodal experts for cancer survival prediction. In *International Conference on Medical Image Computing and Computer-Assisted Intervention*, pages 318–328. Springer, 2024.
- [50] Conghao Xiong, Yi Lin, Hao Chen, Hao Zheng, Dong Wei, Yefeng Zheng, Joseph J. Y. Sung, and Irwin King. Takt: Target-aware knowledge transfer for whole slide image classification. In *International Conference on Medical Image Computing and Computer-Assisted Intervention*, pages 503–513. Springer, 2024.
- [51] Yingxue Xu, Yihui Wang, Fengtao Zhou, Jiabo Ma, Shu Yang, Huangjing Lin, Xin Wang, Jiguang Wang, Li Liang, Anjia Han, et al. A multimodal knowledge-enhanced whole-slide pathology foundation model. *arXiv preprint arXiv:2407.15362*, 2024.
- [52] Hongrun Zhang, Yanda Meng, Yitian Zhao, Yihong Qiao, Xiaoyun Yang, Sarah E Coupland, and Yalin Zheng. Dtf-d-mil: Double-tier feature distillation multiple instance learning for histopathology whole slide image classification. In *Proceedings of the IEEE/CVF conference on computer vision and pattern recognition*, pages 18802–18812, 2022.
- [53] Yunlong Zhang, Zhongyi Shui, Yunxuan Sun, Honglin Li, Jingxiong Li, Chenglu Zhu, Sunyi Zheng, and Lin Yang. Adr: Attention diversification regularization for mitigating overfitting in multiple instance learning based whole slide image classification. *arXiv e-prints*, pages arXiv–2406, 2024.
- [54] Ziyang Zhang, Yang Yu, Yucheng Chen, Xulei Yang, and Si Yong Yeo. Medunifier: Unifying vision-and-language pre-training on medical data with vision generation task using discrete visual representations. *arXiv preprint arXiv:2503.01019*, 2025.

A Derivations for Time Complexity Analysis

We begin by analyzing a general case time complexity and then use the result to analyze our method.

In this section, we derive the computational cost of both the forward and backward passes through a single linear layer. We show that each pass scales linearly with the total number of weights $d_0 d_1$.

For convenience of the following derivations, we define the notations as follows,

$$M = [M_{ij}] \in \mathbb{R}^{d_0 \times d_1}, \quad (7)$$

$$x = [x_j] \in \mathbb{R}^{d_0}, \quad (8)$$

$$z = Mx = [z_i] \in \mathbb{R}^{d_1}, \quad (9)$$

$$\delta = \nabla_z L = [\delta_i] \in \mathbb{R}^{d_1}. \quad (10)$$

A.1 Forward Pass

To compute the pre-activation vector z , each component z_i performs a dot product between the i th row of M and the input x , the z_i is given by,

$$z_i = \sum_{j=1}^{d_0} M_{ij} x_j. \quad (11)$$

Since there are d_1 such outputs and each requires d_0 multiplications (and roughly the same number of additions), the total cost of the forward pass is $\mathcal{O}(d_0 d_1)$.

A.2 Backward Pass

The backward pass consists of three main steps: computing the gradient with respect to the weights, propagating the gradient to the inputs, and updating the weights.

Weight Gradients The derivative of the loss L with respect to each weight M_{ij} follows by the chain rule, is given by,

$$\frac{\partial L}{\partial M_{ij}} = \frac{\partial L}{\partial z_i} \frac{\partial z_i}{\partial M_{ij}} = \delta_i \cdot x_j. \quad (12)$$

Collecting these into the full gradient matrix yields the outer product,

$$\nabla_M L = \delta x^\top, \quad (13)$$

which requires computing one scalar product for each of the $d_0 d_1$ entries. Hence, the cost of this step is $\mathcal{O}(d_0 d_1)$.

Input Gradients To propagate the error back into the input space, we compute,

$$\nabla_x L = M^\top \delta. \quad (14)$$

This is a matrix–vector product of dimensions $d_0 \times d_1$, again costing $\mathcal{O}(d_0 d_1)$.

Weight Update A typical gradient descent update modifies each entry of M by

$$M_{ij} \leftarrow M_{ij} - \eta \frac{\partial L}{\partial M_{ij}}. \quad (15)$$

Updating all $d_0 d_1$ weights elementwise thus costs

$$\mathcal{O}(d_0 d_1). \quad (16)$$

A.3 Total Time Complexity

Summing the costs of the forward pass and all backward-pass components, we obtain $\mathcal{O}(d_0 d_1)$ complexity. Therefore, a single backpropagation step for one example in this layer has time complexity linear in the number of parameters $d_0 d_1$.

B Proof of Random Recalibration Matrix Preserving Input Characteristics

We categorize the geometric characteristics of the input features into variance and covariance; inner products and norms; cosine similarity; pairwise distances; condition numbers; the restricted isometry property; subspace embeddings; manifold geometry; cluster structure; nearest-neighbor relationships; and simplex volumes. We then demonstrate that each of these properties satisfies precise invariance conditions, ensuring that the recalibration matrix preserves the underlying geometric structure.

In this proof, we take the Kaiming uniform initialization with $a = \sqrt{5}$ as an example, which is the default initialization method for linear layers.

B.1 Variance and Covariance Preservation

Intuitively, this result says that when you multiply your data covariance by a “random” matrix M , all of the original variance spreads out evenly across the new d_1 dimensions, up to the constant factor $d_1/(3 d_0)$. In other words, no particular direction in the original space is biased on average.

To derive the scaling of total variance under projection, we start from,

$$\text{tr}(M^\top \Sigma M) = \sum_{p=1}^{d_1} (M^\top \Sigma M)_{pp} = \sum_{p=1}^{d_1} \sum_{q=1}^{d_0} \sum_{r=1}^{d_0} M_{q,p} \Sigma_{q,r} M_{r,p}. \quad (17)$$

Taking expectation and using linearity gives,

$$E[\text{tr}(M^\top \Sigma M)] = \sum_{p=1}^{d_1} \sum_{q=1}^{d_0} \sum_{r=1}^{d_0} \Sigma_{q,r} E[M_{q,p} M_{r,p}]. \quad (18)$$

Because the entries $M_{q,p}$ are independent with $E[M_{q,p}] = 0$, only terms with $q = r$ survive:

$$E[M_{q,p} M_{r,p}] = \begin{cases} \text{Var}(M_{q,p}) = \frac{1}{3 d_0}, & q = r, \\ 0, & q \neq r. \end{cases} \quad (19)$$

Substituting back, we have,

$$E[\text{tr}(M^\top \Sigma M)] = \sum_{p=1}^{d_1} \sum_{q=1}^{d_0} \Sigma_{q,q} \frac{1}{3 d_0} = \frac{d_1}{3 d_0} \sum_{q=1}^{d_0} \Sigma_{q,q} = \frac{d_1}{3 d_0} \text{tr}(\Sigma). \quad (20)$$

B.2 Inner Products and Norms

A random projection with independent, zero-mean entries treats every coordinate of the vectors in an unbiased way. On average, the dot product between any two vectors u and v are scaled by the factor $d_1/(3 d_0)$, and its sign and relative magnitude remain the same. Geometrically, this means angles and lengths are preserved in expectation, no particular direction in the original space is preferred, and so the overall similarity structure of the data survives the embedding up to a known scale.

To see how pairwise inner products scale, we write,

$$\langle M u, M v \rangle = \sum_{p=1}^{d_1} (M u)_p (M v)_p = \sum_{p=1}^{d_1} \sum_{i=1}^{d_0} \sum_{j=1}^{d_0} M_{p,i} u_i M_{p,j} v_j. \quad (21)$$

Taking expectation, and we have,

$$E[\langle M u, M v \rangle] = \sum_{p,i,j} u_i v_j E[M_{p,i} M_{p,j}]. \quad (22)$$

By independence and zero mean, only $i = j$ terms contribute:

$$E[M_{p,i} M_{p,j}] = \begin{cases} \frac{1}{3 d_0}, & i = j, \\ 0, & i \neq j, \end{cases} \quad (23)$$

therefore, we have,

$$E[\langle M u, M v \rangle] = \sum_{p=1}^{d_1} \sum_{i=1}^{d_0} u_i v_i \frac{1}{3 d_0} = \frac{d_1}{3 d_0} \langle u, v \rangle. \quad (24)$$

Similarly, the norm squared follows as the special case $u = v$,

$$E[\|M u\|^2] = E[\langle M u, M u \rangle] = \frac{d_1}{3 d_0} \|u\|^2. \quad (25)$$

B.3 Cosine Similarity

Cosine similarity measures only the angle between two vectors, not their lengths. Since the random projection scales all lengths and dot products by the same constant in expectation, it does not distort angles on average. In effect, no particular direction is stretched more than any other, so the typical cosine similarity between any two points remains exactly as it was before projection.

Since both inner products and norms incur the same factor $\frac{d_1}{3 d_0}$ in expectation, the mean cosine similarity is exactly preserved:

$$E[\cos \theta'] = \frac{E[\langle M u, M v \rangle]}{\sqrt{E[\|M u\|^2] E[\|M v\|^2]}} = \frac{\frac{d_1}{3 d_0} \langle u, v \rangle}{\sqrt{\frac{d_1}{3 d_0} \|u\|^2 \frac{d_1}{3 d_0} \|v\|^2}} = \cos \theta. \quad (26)$$

B.4 Pairwise Distances

This property guarantees that a random projection will maintain the original distances between every pair of data points up to a small, controllable error with high likelihood. In effect, the projection spreads each original distance across many independent components, and by concentration of measure those components collectively reproduce the true separation very closely. As a result, one can embed high-dimensional data into a much lower-dimensional space without significantly distorting the geometric relationships, ensuring that algorithms relying on inter-point distances, such as clustering or nearest-neighbor retrieval, continue to perform reliably.

Let $v = x_i - x_j$. Then

$$\|M v\|^2 = \sum_{p=1}^{d_1} \left(\sum_{q=1}^{d_0} M_{p,q} v_q \right)^2. \quad (27)$$

Define for each p ,

$$Y_p = \sum_{q=1}^{d_0} M_{p,q} v_q, \quad E[Y_p] = 0, \quad \text{Var}(Y_p) = \frac{\|v\|^2}{3 d_0}. \quad (28)$$

By concentration of $\sum_p Y_p^2$, with probability $\geq 1 - \delta$,

$$(1 - \varepsilon) \|v\|^2 \leq \|M v\|^2 \leq (1 + \varepsilon) \|v\|^2, \text{ if } d_1 \geq C \varepsilon^{-2} \ln(N/\delta). \quad (29)$$

B.5 Condition Number

This property ensures that a random projection will not substantially worsen the numerical stability of the data. In other words, the projection maintains the balance between the directions in which the data stretches the most and the least. As a result, any algorithms that depend on solving linear systems or performing matrix decompositions will continue to behave reliably after projection, because the projected matrix remains nearly as well-conditioned as the original. This property is especially important in neural networks, as the performance of them heavily rely on the numerical stability.

For data matrix X and any unit u ,

$$\|X M u\|^2 = u^\top M^\top X^\top X M u. \quad (30)$$

Applying matrix concentration on $X M$ shows that if

$$d_1 \geq C \varepsilon^{-2} d_0, \quad (31)$$

Table 6: Ablation studies of our proposed method across varying shot settings on the Camelyon16, TCGA-NSCLC, and TCGA-RCC datasets. Metrics highlighted in bold red indicate the top result, while those in italicized blue denote the second-best result.

#S	Methods	#P	Camelyon16			TCGA-NSCLC			TCGA-RCC		
			AUC \uparrow	F1 \uparrow	Acc. \uparrow	AUC \uparrow	F1 \uparrow	Acc. \uparrow	AUC \uparrow	F1 \uparrow	Acc. \uparrow
1	Ours	0.17	0.638 _{0.053}	<i>0.531</i> _{0.100}	0.607 _{0.070}	<i>0.628</i> _{0.074}	0.556 _{0.047}	0.567 _{0.048}	0.909 _{0.024}	0.799 _{0.029}	0.813 _{0.043}
	- SP	0.01	0.631 _{0.052}	0.506 _{0.116}	0.649 _{0.027}	0.624 _{0.105}	0.572 _{0.158}	<i>0.577</i> _{0.154}	0.845 _{0.058}	0.675 _{0.145}	0.675 _{0.178}
	- Random	0.17	0.525 _{0.111}	0.275 _{0.000}	0.380 _{0.000}	0.328 _{0.032}	0.341 _{0.013}	0.409 _{0.006}	0.613 _{0.191}	0.201 _{0.100}	0.306 _{0.152}
	- GELU	0.17	0.635 _{0.162}	0.528 _{0.097}	0.607 _{0.070}	0.594 _{0.077}	0.511 _{0.103}	0.544 _{0.076}	0.906 _{0.028}	0.793 _{0.039}	0.803 _{0.043}
	ReLU	0.17	0.638 _{0.054}	0.530 _{0.097}	0.607 _{0.070}	0.585 _{0.091}	0.540 _{0.091}	0.553 _{0.081}	<i>0.907</i> _{0.021}	<i>0.798</i> _{0.023}	<i>0.812</i> _{0.035}
	Sigmoid	0.17	0.635 _{0.054}	0.526 _{0.104}	0.612 _{0.074}	0.570 _{0.096}	0.553 _{0.085}	0.560 _{0.077}	0.887 _{0.044}	0.713 _{0.121}	0.711 _{0.154}
	Tanh	0.17	<i>0.637</i> _{0.053}	0.534 _{0.100}	<i>0.610</i> _{0.066}	0.654 _{0.046}	<i>0.569</i> _{0.064}	0.592 _{0.038}	0.890 _{0.045}	0.749 _{0.126}	0.746 _{0.154}
2	Ours	0.17	<i>0.682</i> _{0.053}	0.571 _{0.164}	0.674 _{0.104}	0.951 _{0.002}	<i>0.861</i> _{0.014}	<i>0.862</i> _{0.013}	<i>0.989</i> _{0.003}	<i>0.889</i> _{0.002}	<i>0.916</i> _{0.007}
	- SP	0.01	0.509 _{0.106}	0.457 _{0.033}	0.597 _{0.048}	0.840 _{0.024}	0.768 _{0.015}	0.768 _{0.015}	0.958 _{0.006}	0.814 _{0.017}	0.852 _{0.016}
	- Random	0.17	0.525 _{0.111}	0.275 _{0.000}	0.380 _{0.000}	0.328 _{0.032}	0.341 _{0.022}	0.404 _{0.011}	0.613 _{0.191}	0.203 _{0.109}	0.309 _{0.160}
	- GELU	0.17	0.674 _{0.162}	<i>0.569</i> _{0.146}	0.661 _{0.126}	0.939 _{0.011}	0.858 _{0.018}	0.858 _{0.018}	0.990 _{0.002}	0.890 _{0.011}	0.922 _{0.009}
	ReLU	0.17	0.667 _{0.097}	0.531 _{0.098}	0.630 _{0.037}	<i>0.945</i> _{0.012}	0.856 _{0.020}	0.857 _{0.020}	<i>0.989</i> _{0.002}	0.887 _{0.009}	0.913 _{0.007}
	Sigmoid	0.17	0.685 _{0.105}	0.539 _{0.154}	<i>0.672</i> _{0.057}	0.939 _{0.013}	0.859 _{0.018}	0.859 _{0.017}	<i>0.979</i> _{0.012}	0.875 _{0.018}	0.902 _{0.020}
	Tanh	0.17	0.663 _{0.108}	0.465 _{0.088}	0.610 _{0.038}	0.929 _{0.008}	0.864 _{0.010}	0.864 _{0.010}	0.976 _{0.012}	0.852 _{0.025}	0.883 _{0.026}
4	Ours	0.17	<i>0.801</i> _{0.032}	0.765 _{0.028}	0.786 _{0.029}	0.946 _{0.006}	0.884 _{0.003}	0.884 _{0.003}	0.988 _{0.000}	0.916 _{0.004}	0.934 _{0.002}
	- SP	0.01	0.445 _{0.011}	0.472 _{0.019}	0.579 _{0.035}	0.839 _{0.012}	0.758 _{0.014}	0.758 _{0.014}	0.958 _{0.005}	0.837 _{0.023}	0.859 _{0.026}
	- Random	0.17	0.525 _{0.111}	0.275 _{0.000}	0.380 _{0.000}	0.328 _{0.032}	0.341 _{0.017}	0.407 _{0.004}	0.613 _{0.191}	0.204 _{0.108}	0.311 _{0.160}
	- GELU	0.17	0.734 _{0.020}	0.710 _{0.036}	0.742 _{0.044}	0.882 _{0.065}	0.819 _{0.063}	0.819 _{0.063}	0.988 _{0.001}	0.909 _{0.004}	0.930 _{0.002}
	ReLU	0.17	0.808 _{0.031}	<i>0.756</i> _{0.033}	<i>0.775</i> _{0.034}	0.905 _{0.064}	0.845 _{0.061}	0.845 _{0.061}	0.988 _{0.000}	<i>0.913</i> _{0.010}	<i>0.932</i> _{0.007}
	Sigmoid	0.17	0.700 _{0.038}	0.616 _{0.042}	0.630 _{0.054}	<i>0.936</i> _{0.022}	<i>0.869</i> _{0.033}	<i>0.869</i> _{0.032}	0.986 _{0.001}	0.901 _{0.015}	0.916 _{0.017}
	Tanh	0.17	0.699 _{0.057}	0.648 _{0.025}	0.672 _{0.022}	0.919 _{0.045}	0.851 _{0.042}	0.852 _{0.042}	<i>0.987</i> _{0.000}	0.912 _{0.015}	<i>0.932</i> _{0.009}
8	Ours	0.17	0.858 _{0.021}	0.824 _{0.005}	0.848 _{0.004}	0.950 _{0.010}	0.896 _{0.013}	0.896 _{0.013}	0.994 _{0.002}	0.940 _{0.004}	0.950 _{0.002}
	- SP	0.01	0.595 _{0.017}	0.439 _{0.098}	0.633 _{0.022}	0.906 _{0.013}	0.826 _{0.019}	0.826 _{0.019}	0.974 _{0.003}	0.892 _{0.021}	0.902 _{0.013}
	- Random	0.17	0.525 _{0.111}	0.275 _{0.000}	0.380 _{0.000}	0.328 _{0.032}	0.343 _{0.015}	0.401 _{0.012}	0.613 _{0.191}	0.204 _{0.101}	0.309 _{0.154}
	- GELU	0.17	0.822 _{0.029}	0.793 _{0.038}	0.822 _{0.031}	<i>0.951</i> _{0.007}	0.902 _{0.006}	0.902 _{0.006}	0.988 _{0.001}	<i>0.939</i> _{0.001}	0.950 _{0.002}
	ReLU	0.17	0.840 _{0.031}	0.823 _{0.032}	0.845 _{0.027}	0.955 _{0.002}	0.906 _{0.008}	0.906 _{0.008}	<i>0.992</i> _{0.001}	<i>0.939</i> _{0.005}	<i>0.948</i> _{0.005}
	Sigmoid	0.17	0.810 _{0.021}	0.719 _{0.079}	0.729 _{0.084}	0.947 _{0.001}	<i>0.905</i> _{0.010}	<i>0.905</i> _{0.010}	0.990 _{0.000}	0.883 _{0.022}	0.910 _{0.017}
	Tanh	0.17	0.789 _{0.020}	0.752 _{0.089}	0.767 _{0.097}	0.950 _{0.004}	0.900 _{0.004}	0.900 _{0.004}	0.990 _{0.003}	0.934 _{0.004}	0.943 _{0.005}
16	Ours	0.17	0.941 _{0.004}	<i>0.876</i> _{0.021}	<i>0.884</i> _{0.023}	0.970 _{0.003}	0.920 _{0.011}	0.920 _{0.011}	0.998 _{0.000}	0.960 _{0.007}	0.967 _{0.005}
	- SP	0.01	0.561 _{0.018}	0.550 _{0.013}	0.656 _{0.022}	0.938 _{0.013}	0.883 _{0.019}	0.883 _{0.019}	0.986 _{0.001}	0.897 _{0.015}	0.919 _{0.011}
	- Random	0.17	0.525 _{0.111}	0.274 _{0.002}	0.377 _{0.004}	0.328 _{0.032}	0.345 _{0.016}	0.384 _{0.017}	0.614 _{0.191}	0.213 _{0.099}	0.311 _{0.154}
	- GELU	0.17	0.938 _{0.013}	0.872 _{0.005}	0.876 _{0.004}	0.967 _{0.002}	<i>0.918</i> _{0.014}	<i>0.918</i> _{0.014}	<i>0.997</i> _{0.000}	0.950 _{0.011}	0.959 _{0.007}
	ReLU	0.17	0.939 _{0.003}	0.887 _{0.023}	0.894 _{0.024}	<i>0.968</i> _{0.003}	0.916 _{0.014}	0.916 _{0.014}	<i>0.997</i> _{0.000}	<i>0.959</i> _{0.011}	<i>0.966</i> _{0.009}
	Sigmoid	0.17	0.778 _{0.061}	0.698 _{0.075}	0.713 _{0.084}	0.956 _{0.004}	0.905 _{0.012}	0.905 _{0.012}	0.988 _{0.006}	0.919 _{0.022}	0.922 _{0.015}
	Tanh	0.17	0.806 _{0.032}	0.568 _{0.145}	0.584 _{0.126}	0.615 _{0.105}	0.570 _{0.098}	0.575 _{0.095}	0.882 _{0.013}	0.748 _{0.005}	0.771 _{0.013}

then with high probability

$$(1 - \varepsilon) u^\top X^\top X u \leq u^\top M^\top X^\top X M u \leq (1 + \varepsilon) u^\top X^\top X u, \quad (32)$$

so

$$\kappa(XM) \leq \frac{1 + \varepsilon}{1 - \varepsilon} \kappa(X) \approx (1 + \varepsilon) \kappa(X). \quad (33)$$

B.6 Restricted Isometry Property

This property ensures that a random projection acts almost like a perfect length-preserver on all sparse vectors at once. In practice, it means that if the data has an underlying sparse structure, we can compress it drastically without losing the ability to tell sparse signals apart or to reconstruct them reliably. By making the projection dimension grow in line with how many nonzeros we expect, we guard against any sparse pattern being overly distorted.

For any K -sparse x ,

$$\|Mx\|^2 = \sum_{p=1}^{d_1} \left(\sum_{q \in \text{supp}(x)} M_{p,q} x_q \right)^2. \quad (34)$$

A union bound over all supports yields that if

$$d_1 \geq C \delta^{-2} K \ln \frac{d_0}{K}, \quad (35)$$

Table 7: Performance of ABMIL with replaced linear layers under varying shot settings on Camelyon16, TCGA-NSCLC, and TCGA-RCC datasets. “U” and “V” denote two matrices in ABMIL.

#S	Methods	#P	Camelyon16			TCGA-NSCLC			TCGA-RCC		
			AUC↑	F1↑	Acc.↑	AUC↑	F1↑	Acc.↑	AUC↑	F1↑	Acc.↑
4	V	0.18	0.749 _{0.019}	0.720 _{0.011}	0.749 _{0.016}	0.924 _{0.038}	0.855 _{0.050}	0.855 _{0.050}	0.982 _{0.001}	0.889 _{0.017}	0.909 _{0.017}
	U	0.17	0.721 _{0.031}	0.717 _{0.013}	0.770 _{0.004}	0.882 _{0.094}	0.819 _{0.120}	0.820 _{0.118}	0.948 _{0.024}	0.819 _{0.023}	0.852 _{0.026}
	V + U	0.17	0.680 _{0.013}	0.682 _{0.007}	0.734 _{0.009}	0.925 _{0.030}	0.866 _{0.044}	0.867 _{0.044}	0.985 _{0.001}	0.913 _{0.009}	0.933 _{0.007}
8	V	0.18	0.850 _{0.011}	0.796 _{0.012}	0.829 _{0.008}	0.953 _{0.015}	0.896 _{0.016}	0.896 _{0.016}	0.986 _{0.003}	0.923 _{0.011}	0.937 _{0.012}
	U	0.17	0.837 _{0.038}	0.776 _{0.046}	0.814 _{0.034}	0.924 _{0.039}	0.855 _{0.060}	0.856 _{0.059}	0.961 _{0.030}	0.853 _{0.035}	0.873 _{0.037}
	V + U	0.17	0.846 _{0.025}	0.797 _{0.028}	0.829 _{0.021}	0.948 _{0.007}	0.892 _{0.029}	0.892 _{0.029}	0.988 _{0.002}	0.926 _{0.003}	0.939 _{0.002}
16	V	0.18	0.901 _{0.030}	0.860 _{0.050}	0.873 _{0.044}	0.971 _{0.003}	0.920 _{0.010}	0.920 _{0.010}	0.995 _{0.000}	0.932 _{0.008}	0.943 _{0.006}
	U	0.17	0.919 _{0.029}	0.888 _{0.031}	0.899 _{0.027}	0.963 _{0.003}	0.919 _{0.010}	0.919 _{0.010}	0.989 _{0.004}	0.913 _{0.011}	0.934 _{0.010}
	V + U	0.17	0.879 _{0.020}	0.826 _{0.005}	0.837 _{0.008}	0.971 _{0.002}	0.925 _{0.002}	0.925 _{0.002}	0.996 _{0.001}	0.950 _{0.002}	0.954 _{0.002}

then for all K -sparse x ,

$$(1 - \delta) \|x\|^2 \leq \|Mx\|^2 \leq (1 + \delta) \|x\|^2. \quad (36)$$

B.7 Subspace Embedding

This property guarantees that a random projection acts as a near-perfect isometric embedding for any fixed low-dimensional subspace. It means that all geometric relationships, lengths and angles, within that subspace are preserved almost exactly after compression. As a result, any downstream algorithm that relies on the subspace structure (for example, solving linear least-squares problems or performing spectral decompositions) will perform almost identically in the reduced space, yet with greatly reduced computational and storage costs.

For a d -dimensional subspace with basis $A \in \mathbb{R}^{d_0 \times d}$, one shows with a net argument that if

$$d_1 = O(\varepsilon^{-2} d), \quad (37)$$

then with high probability

$$(1 - \varepsilon) A^\top A \preceq A^\top M^\top M A \preceq (1 + \varepsilon) A^\top A. \quad (38)$$

B.8 Manifold Geometry

This property ensures that a random projection will faithfully reproduce the intrinsic geometry of any low-dimensional manifold embedded in high-dimensional space. Even though the data may lie on a curved, nonlinear surface, we can compress it down to far fewer dimensions and still retain nearly all of the true “geodesic” distances along that surface. The key idea is that the manifold can be approximated by a finite set of local patches, and the projection preserves each patch’s geometry so accurately that the entire shape remains intact. As a result, analyses that rely on the manifold’s structure, such as nonlinear dimensionality reduction or manifold-based learning, remain valid and effective after compression.

Cover a d -dimensional manifold of volume V by $N \approx (V/\tau)^d$ balls. If

$$d_1 \geq C \varepsilon^{-2} d \ln \frac{V}{\tau}, \quad (39)$$

then all geodesic distances are preserved within $1 \pm \varepsilon$.

B.9 Cluster Labels

This criterion ensures that the worst-case contraction of the gap between clusters still exceeds the worst-case expansion of each cluster’s size. In practice it means that random projection will not cause any overlap between clusters that were originally well separated. As a result, any clustering or classification based on distance remains unchanged, and all original labels are preserved.

Clusters of diameter D separated by Δ satisfy label preservation if

$$(1 - \varepsilon) \Delta > (1 + \varepsilon) D. \quad (40)$$

Table 8: Experimental results on different initialization methods in TransMIL under various shot settings across Camelyon16, TCGA-NSCLC and TCGA-RCC dataset. “K.” stands for Kaiming initialization, “X” stands for Xavier initialization, “U.” stands for uniform distribution, and the number following is the input parameter for initialization.

k	Methods	Camelyon16			TCGA-NSCLC			TCGA-RCC		
		AUC \uparrow	F1 \uparrow	Acc. \uparrow	AUC \uparrow	F1 \uparrow	Acc. \uparrow	AUC \uparrow	F1 \uparrow	Acc. \uparrow
4	K. U. $\sqrt{5}$	0.570 _{0.110}	0.509 _{0.104}	0.550 _{0.116}	0.915 _{0.003}	0.847 _{0.021}	0.847 _{0.022}	0.980 _{0.002}	0.863 _{0.009}	0.895 _{0.002}
	K. U. 0	0.446 _{0.077}	0.419 _{0.036}	0.509 _{0.113}	0.872 _{0.025}	0.786 _{0.049}	0.787 _{0.049}	0.968 _{0.005}	0.845 _{0.023}	0.868 _{0.024}
	K. N. 0	0.427 _{0.061}	0.422 _{0.031}	0.468 _{0.078}	0.711 _{0.194}	0.488 _{0.268}	0.599 _{0.173}	0.500 _{0.000}	0.238 _{0.000}	0.556 _{0.000}
	X. U. 1	0.406 _{0.038}	0.408 _{0.015}	0.429 _{0.004}	0.754 _{0.221}	0.645 _{0.265}	0.703 _{0.165}	0.499 _{0.002}	0.186 _{0.045}	0.396 _{0.138}
	X. G. 1	0.410 _{0.046}	0.427 _{0.036}	0.465 _{0.076}	0.886 _{0.018}	0.810 _{0.036}	0.810 _{0.036}	0.973 _{0.004}	0.862 _{0.013}	0.882 _{0.015}
8	K. U. $\sqrt{5}$	0.885 _{0.042}	0.795 _{0.042}	0.817 _{0.044}	0.948 _{0.001}	0.876 _{0.009}	0.876 _{0.009}	0.988 _{0.004}	0.911 _{0.013}	0.923 _{0.009}
	K. U. 0	0.623 _{0.165}	0.564 _{0.140}	0.571 _{0.150}	0.926 _{0.003}	0.848 _{0.021}	0.848 _{0.021}	0.821 _{0.278}	0.679 _{0.382}	0.791 _{0.204}
	K. N. 0	0.670 _{0.124}	0.597 _{0.163}	0.605 _{0.175}	0.644 _{0.249}	0.512 _{0.310}	0.624 _{0.214}	0.660 _{0.278}	0.449 _{0.364}	0.664 _{0.188}
	X. U. 1	0.730 _{0.135}	0.687 _{0.160}	0.705 _{0.175}	0.931 _{0.013}	0.860 _{0.018}	0.861 _{0.018}	0.816 _{0.274}	0.683 _{0.385}	0.796 _{0.209}
	X. G. 1	0.559 _{0.046}	0.498 _{0.065}	0.504 _{0.061}	0.939 _{0.021}	0.879 _{0.029}	0.880 _{0.029}	0.822 _{0.279}	0.678 _{0.381}	0.791 _{0.204}
16	K. U. $\sqrt{5}$	0.944 _{0.007}	0.887 _{0.044}	0.899 _{0.034}	0.962 _{0.001}	0.901 _{0.004}	0.901 _{0.004}	0.993 _{0.002}	0.949 _{0.005}	0.952 _{0.002}
	K. U. 0	0.901 _{0.063}	0.873 _{0.067}	0.881 _{0.063}	0.652 _{0.263}	0.525 _{0.322}	0.641 _{0.222}	0.986 _{0.007}	0.900 _{0.016}	0.920 _{0.015}
	K. N. 0	0.916 _{0.053}	0.841 _{0.040}	0.855 _{0.031}	0.486 _{0.025}	0.339 _{0.000}	0.513 _{0.000}	0.663 _{0.282}	0.460 _{0.385}	0.676 _{0.210}
	X. U. 1	0.933 _{0.030}	0.868 _{0.027}	0.879 _{0.027}	0.804 _{0.263}	0.713 _{0.323}	0.771 _{0.223}	0.656 _{0.289}	0.443 _{0.423}	0.605 _{0.317}
	X. G. 1	0.930 _{0.045}	0.873 _{0.051}	0.884 _{0.048}	0.956 _{0.004}	0.900 _{0.006}	0.900 _{0.006}	0.919 _{0.123}	0.684 _{0.386}	0.801 _{0.212}

B.10 Nearest Neighbors

The nearest-neighbor property refers to the guarantee that, after random projection, each point’s set of k closest points (its k -nearest-neighbor graph) remains exactly the same as in the original high-dimensional space.

Fast JL transforms $M = PHD$ satisfy the same distortion bounds and run in time $O(d_0 \log d_0 + d_1)$; the k -NN graph is unchanged if

$$\varepsilon < \frac{\gamma}{2D}. \quad (41)$$

B.11 Simplex Volume

A simplex in this context is the most elementary convex polytope determined by one “base” point together with a set of other points that do not all lie in a lower-dimensional subspace. In two dimensions it is a triangle, in three it is a tetrahedron, and in higher dimensions the generalization of those. Its volume quantifies the amount of space enclosed by those corner points. Because the projection acts almost as an exact length-preserver on each independent direction in the simplex, the total enclosed volume can only change by the small, precisely bounded factor implied by the near-isometry.

For $d + 1$ affinely independent points,

$$\text{Vol}(\Delta) = \frac{1}{d!} |\det[x_1 - x_0, \dots, x_d - x_0]|. \quad (42)$$

Since M is an approximate isometry on this d -dimensional span, its singular values lie in $[\sqrt{1 - \varepsilon}, \sqrt{1 + \varepsilon}]$, giving

$$(1 - \varepsilon)^{d/2} \text{Vol}(\Delta) \leq \text{Vol}(\Delta') \leq (1 + \varepsilon)^{d/2} \text{Vol}(\Delta), \quad (43)$$

hence squared volume changes by at most $(1 \pm \varepsilon)^d$.

C Additional Proofs

C.1 Randomly Initialized Matrix Has Full Rank

Theorem 2. Let $W \in \mathbb{R}^{d_0 \times d_1}$ have entries drawn i.i.d. from a continuous distribution (e.g. Kaiming-uniform with gain $\sqrt{5}$). Then with probability one,

$$\text{rank}(W) = \min\{d_0, d_1\}. \quad (44)$$

Table 9: Experimental results on different pretrained feature extractors under various shot settings. “R” stands for ResNet50, “U” stands for UNI, and “L” stands for MIL model with our method.

k	E.	TCGA-NSCLC						TCGA-RCC					
		AUC \uparrow	ABMIL F1 \uparrow	Acc. \uparrow	AUC \uparrow	TransMIL F1 \uparrow	Acc. \uparrow	AUC \uparrow	ABMIL F1 \uparrow	Acc. \uparrow	AUC \uparrow	TransMIL F1 \uparrow	Acc. \uparrow
4	R	0.664 _{0.130}	0.583 _{0.088}	0.597 _{0.089}	0.627 _{0.061}	0.579 _{0.069}	0.589 _{0.063}	0.807 _{0.040}	0.613 _{0.056}	0.623 _{0.058}	0.925 _{0.012}	0.715 _{0.062}	0.752 _{0.052}
	RL	0.701 _{0.008}	0.616 _{0.022}	0.626 _{0.017}	0.580 _{0.065}	0.570 _{0.043}	0.574 _{0.044}	0.873 _{0.009}	0.702 _{0.021}	0.715 _{0.026}	0.933 _{0.018}	0.748 _{0.017}	0.779 _{0.024}
	U	0.756 _{0.014}	0.682 _{0.023}	0.684 _{0.021}	0.832 _{0.002}	0.732 _{0.017}	0.734 _{0.015}	0.968 _{0.025}	0.842 _{0.053}	0.870 _{0.040}	0.976 _{0.001}	0.836 _{0.003}	0.863 _{0.004}
	UL	0.872 _{0.038}	0.793 _{0.049}	0.793 _{0.048}	0.842 _{0.046}	0.757 _{0.014}	0.758 _{0.049}	0.974 _{0.020}	0.861 _{0.026}	0.885 _{0.023}	0.979 _{0.003}	0.847 _{0.014}	0.868 _{0.013}
8	R	0.666 _{0.037}	0.627 _{0.016}	0.627 _{0.017}	0.692 _{0.054}	0.504 _{0.127}	0.574 _{0.061}	0.839 _{0.018}	0.686 _{0.038}	0.709 _{0.049}	0.868 _{0.055}	0.607 _{0.072}	0.681 _{0.051}
	RL	0.710 _{0.006}	0.668 _{0.009}	0.668 _{0.009}	0.667 _{0.095}	0.523 _{0.116}	0.569 _{0.071}	0.851 _{0.003}	0.699 _{0.019}	0.726 _{0.020}	0.917 _{0.007}	0.743 _{0.019}	0.768 _{0.009}
	U	0.814 _{0.070}	0.746 _{0.076}	0.747 _{0.076}	0.842 _{0.011}	0.761 _{0.006}	0.762 _{0.006}	0.984 _{0.008}	0.901 _{0.053}	0.909 _{0.052}	0.983 _{0.003}	0.890 _{0.017}	0.899 _{0.020}
	UL	0.910 _{0.028}	0.836 _{0.027}	0.837 _{0.027}	0.859 _{0.026}	0.779 _{0.014}	0.779 _{0.014}	0.989 _{0.001}	0.919 _{0.010}	0.927 _{0.004}	0.985 _{0.001}	0.897 _{0.010}	0.902 _{0.007}
16	R	0.618 _{0.037}	0.577 _{0.016}	0.580 _{0.017}	0.590 _{0.027}	0.483 _{0.077}	0.540 _{0.029}	0.745 _{0.072}	0.570 _{0.125}	0.564 _{0.133}	0.752 _{0.055}	0.533 _{0.049}	0.577 _{0.069}
	RL	0.666 _{0.006}	0.635 _{0.010}	0.635 _{0.010}	0.585 _{0.011}	0.538 _{0.054}	0.556 _{0.028}	0.814 _{0.045}	0.629 _{0.046}	0.625 _{0.049}	0.873 _{0.045}	0.696 _{0.075}	0.711 _{0.091}
	U	0.891 _{0.040}	0.843 _{0.031}	0.843 _{0.031}	0.892 _{0.042}	0.814 _{0.037}	0.815 _{0.038}	0.993 _{0.001}	0.948 _{0.011}	0.953 _{0.013}	0.994 _{0.001}	0.945 _{0.013}	0.950 _{0.016}
	UL	0.945 _{0.005}	0.891 _{0.015}	0.891 _{0.014}	0.907 _{0.017}	0.842 _{0.022}	0.843 _{0.021}	0.995 _{0.002}	0.948 _{0.008}	0.954 _{0.005}	0.995 _{0.001}	0.944 _{0.004}	0.949 _{0.007}

Proof. Set $r = \min\{d_0, d_1\}$. Define the singular set

$$S = \{\mathbf{W} : \text{rank}(\mathbf{W}) < r\}. \quad (45)$$

A matrix in S must make every $r \times r$ minor vanish. Label those minors by index sets I , and write

$$Z_I = \{\mathbf{W} : \det(\mathbf{W}_I) = 0\}. \quad (46)$$

Each \det_I is a nonzero polynomial in the entries of \mathbf{W} , so by basic measure theory its zero set Z_I has Lebesgue measure zero. Since there are finitely many I ,

$$S = \bigcup_I Z_I \quad (47)$$

is a finite union of null sets, hence also null. Finally, the distribution on entries is absolutely continuous with respect to Lebesgue measure, so

$$\Pr(\mathbf{W} \in S) = 0, \quad (48)$$

and therefore \mathbf{W} has full rank r almost surely. \square

C.2 Maximum Rank of the Squeeze Pathway

Theorem 3 (Rank of a Low-Rank Product). *Let $\mathbf{W}_2 \in \mathbb{R}^{m \times r}$ and $\mathbf{W}_1 \in \mathbb{R}^{r \times n}$ with $r < \min(m, n)$. Then*

$$\text{rank}(\mathbf{W}_2 \mathbf{W}_1) \leq r. \quad (49)$$

Proof. Observe that

$$\text{rank}(\mathbf{W}_2) \leq r, \quad \text{rank}(\mathbf{W}_1) \leq r, \quad (50)$$

since \mathbf{W}_2 has only r columns and \mathbf{W}_1 has only r rows. A standard rank-inequality for matrix products states

$$\text{rank}(AB) \leq \min(\text{rank}(A), \text{rank}(B)) \quad (51)$$

for any conformable A, B . Applying this with $A = \mathbf{W}_2$ and $B = \mathbf{W}_1$ gives

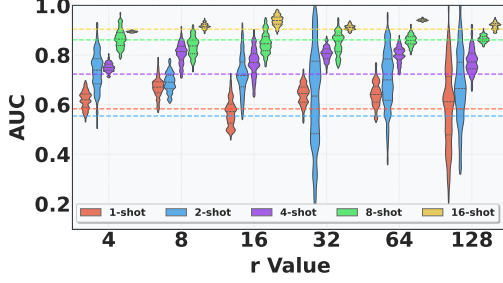
$$\text{rank}(\mathbf{W}_2 \mathbf{W}_1) \leq \min(\text{rank}(\mathbf{W}_2), \text{rank}(\mathbf{W}_1)) \leq r. \quad (52)$$

\square

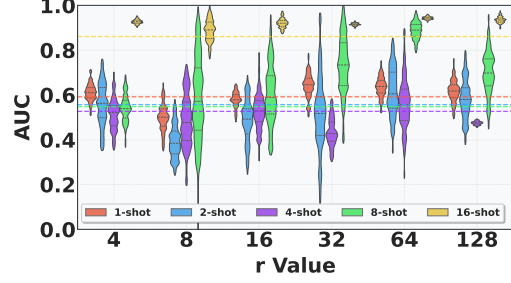
D Experiment Setups

D.1 Dataset Descriptions

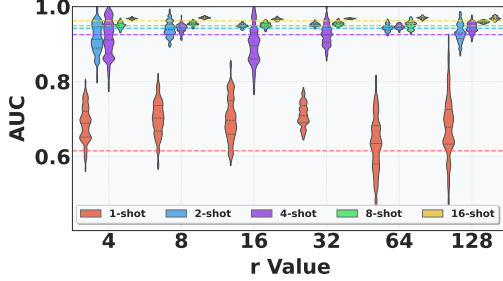
Camelyon16 [30] comprises 397 WSIs of lymph node sections from breast cancer patients, annotated for metastatic presence. The dataset is officially partitioned into 270 training specimens (157 normal, 111 tumor-containing) and 129 testing specimens. For our experimental protocol, we further stratified



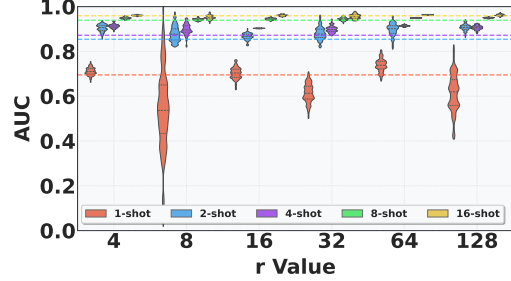
(a) AUC score of LCLAM on Camelyon16.



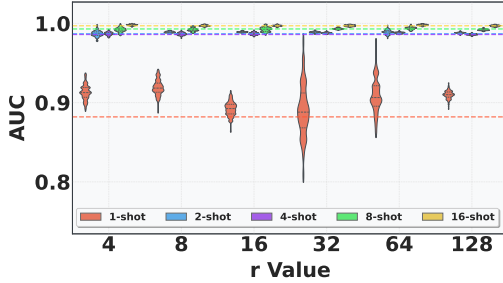
(b) AUC score of LTransMIL on Camelyon16.



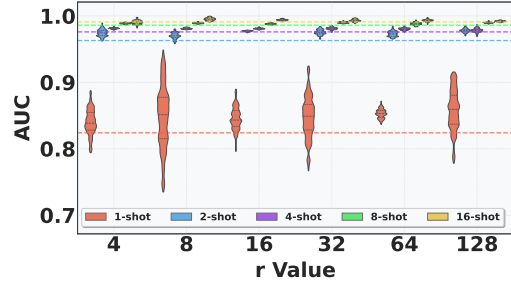
(c) AUC score of LCLAM on NSCLC.



(d) AUC score of LTransMIL on NSCLC.



(e) AUC score of LCLAM on RCC.



(f) AUC score of LTransMIL on RCC.

Figure 4: Sensitivity analysis of parameter r across multiple datasets using LCLAM and LTransMIL. Dashed lines indicate the performance of the respective baseline methods (CLAM and TransMIL).

the training cohort into training and validation subsets using a 7:3 ratio while maintaining the class distribution. All experiments were conducted on the official test set.

TCGA-RCC¹ encompasses 940 WSIs from three distinct renal cell carcinoma subtypes: Kidney Chromophobe (TCGA-KICH, 121 WSIs from 109 cases), Kidney Renal Clear Cell Carcinoma (TCGA-KIRC, 519 WSIs from 513 cases), and Kidney Renal Papillary Cell Carcinoma (TCGA-KIRP, 300 WSIs from 276 cases). We partition the dataset into training, validation, and test sets with proportions of 60%, 15%, and 25%, respectively.

TCGA-NSCLC consists of 1,053 WSIs representing two major lung cancer histological subtypes: Lung Squamous Cell Carcinoma (TCGA-LUSC, 512 WSIs from 478 cases) and Lung Adenocarcinoma (TCGA-LUAD, 541 WSIs from 478 cases). Following the same methodology as for the RCC dataset, we employed a 60:15:25 ratio for training, validation, and test set construction.

¹The TCGA data used in our work is available in <https://portal.gdc.cancer.gov>.

D.2 Computer Resources

We conduct our experiments on an NVIDIA A100 GPU and Intel(R) Xeon(R) Silver 4410Y CPU, with Ubuntu system version 22.04.5 LTS (GNU/Linux 5.15.0-136-generic x86_64). More detailed python environmental information would be released with the code.

D.3 Replacement Position of the Models

ABMIL: replace the V matrix with our SR block.

CLAM²: replace every matrix except for classifier with our SR block.

TransMIL³: only replace the out matrix in nystrom attention implementation with our SR block.

CATE⁴: replace all linear layers in `x_linear`, `interv_linear`, feature output linear layer and the second linear layer in `encoder_TB` with our SR block.

More details will be available along with the code.

E Additional Experimental Results

The additional experimental results are presented in Tables 6 to 9, and Fig. 4. The discussions of these tables and figures are already available in Sec. 4 in the main text.

F Limitations and Future Works

This work introduces an SR block to replace the linear layers in MIL models, thereby mitigating overfitting, suppressing spurious feature learning, and removing the need for complex preprocessing and excessive parameter overhead. However, our empirical evaluation has several limitations. First, we fix the rank r across all layers, a choice that is unlikely to be optimal in real-world scenarios. A more comprehensive exploration of different rank values within a single model would better characterize the trade-off between model size and accuracy. Second, our study of insertion positions is limited to the ABMIL architecture; to establish broader applicability, the SR block should also be tested in more sophisticated MIL frameworks such as TransMIL and CATE. We treat these limitations of our work as future directions of our work.

We anticipate that the proposed SR block will broadly advance few-shot learning both within computational pathology and beyond. Its minimal deployment requirements render it readily applicable in a wide range of settings. In computational pathology, it may enhance tasks such as few-shot report generation, survival outcome prediction, mutation inference, and treatment-response modeling, among others. More generally, the SR block could improve performance in computer vision applications, including few-shot segmentation and classification, and may even be adapted to natural-language-processing tasks. Further exploration across these domains is therefore warranted.

²<https://github.com/mahmoodlab/CLAM>

³<https://github.com/szc19990412/TransMIL>

⁴<https://github.com/HKU-MedAI/CATE>